Chinese Journal of Aeronautics, (2025), 38(9): 103511

Chinese Society of Aeronautics and Astronautics
& Beihang University

Chinese Journal of Aeronautics

cja@buaa.edu.cn
www.sciencedirect.com

FULL LENGTH ARTICLE

Aerodynamic modeling and analysis of aerial-aquatic rotorcraft performance near and crossing the air-water interface

Qi ZHAN [a], Xiao WANG [a,*], Junhui HU [a], Xingzhi BAI [b], Pierangelo MASARATI [c]

[a] National Key Laboratory of Helicopter Aeromechanics, Nanjing University of Aeronautics and Astronautics, Nanjing 210016, China
[b] Cross-media Vehicle Research Center, China Aerodynamics Research and Development Center, Mianyang 621000, China
[c] Department of Aerospace Science and Technology, Politecnico di Milano, Milan 20156, Italy

Received 7 August 2024; revised 13 October 2024; accepted 23 February 2025
Available online 26 March 2025

KEYWORDS

Aerial-auatic rtorcraft;
Ground effect;
Water effect;
Finite vortex rotor model;
Transition boundary

Abstract Blending the agility of aerial drones with the covert capabilities of underwater submersibles, the aerial-aquatic rotorcraft has garnered substantial interest due to their unparalleled capacity to traverse both air and water. Nevertheless, a critical hurdle for these vehicles lies in mitigating the adverse effects of repeatedly transitioning between these environments, particularly during water-surface takeoffs. Currently, research on the interference caused by rotors approaching water surfaces remains limited. This paper introduces a novel adaptive rotor aerodynamic model based on continuous finite vortex theory to predict rotor thrust within gas–liquid flow field. Initially, the model's sensitivity to system parameters was analyzed to optimize its predictive capabilities. Subsequently, a comprehensive ground/water experimental setup was designed to investigate the intricate aerodynamic interactions between the rotor flow field and water. By varying rotor sizes, the characteristics of the rotor flow field and water surface were examined at different rotor-water surface distances. The performance of different modeling methods was analyzed based on the rotor experimental data of a diameter of 0.38 m, and the prediction results were quantified using the percentage of the mean-square error. The results show that the average error of the finite vortex rotor model is the smallest. Finally, a novel transition boundary is proposed to divide the rotor flow field of the gas–liquid mixture into two stages. The thrust loss zone is defined to delineate the safe operating range of the aircraft, providing a basis for the design of aerial-aquatic rotorcraft.

1. Introduction

As science and technology progress at an unprecedented pace[1] and ocean exploration activities diversify,[2,3] Aerial-Aquatic Rotorcraft (AAR) have emerged as a captivating area of research due to their unique capability to execute a wide range

* Corresponding author.
E-mail address: x.wang@nuaa.edu.cn (X. WANG).
Peer review under responsibility of Editorial Committee of CJA

Production and hosting by Elsevier

https://doi.org/10.1016/j.cja.2025.103511
1000-9361

of missions in both aerial and aquatic environments, including reconnaissance, communication relay, and underwater search and rescue. AAR seamlessly integrate the strengths of drones and underwater vehicles, enabling them to fly in the air and navigate underwater without additional mission complexity. They are widely regarded as a transformative technology proposed to break through the limitations of drone applications.[1,4,5] However, there is no existing AAR that can simultaneously retain the maneuverability of both drones and underwater vehicles without compromising its own performance.

Among the plethora of aerial-aquatic rotorcraft, those employing rotors have emerged as the frontrunners due to their advantages in terms of continuous thrust, robust air–water compatibility, and the ability to hover, which have made them the preferred option in this domain.[1] Accordingly, many researchers have dedicated their efforts to the aerodynamic modeling and control of aerial-aquatic rotorcraft, e.g., Li et al.,[6] Villegas et al.,[7] Lu et al.,[8] Horn et al.,[9,10] Weisler et al.,[11] etc. However, a pervasive oversight in these investigations is the disregard for the substantial influence of the water-surface interference on the performance of aerial-aquatic rotorcraft. Additionally, there is a lack of attention devoted to the near-water phenomena that occur during the transition phase between water and air.[12] In some instances, the water surface interference has been erroneously considered equivalent to the ground effect.[13]

As a critical component of rotorcraft vehicles, rotors are responsible for providing precise thrust and flexible attitude control.[14] When an AAR approaches an object, the object obstructs and alters the flow of the rotor wake, which leads to a change in the flow field and subsequently affects the aerodynamic performance of the rotor. Currently, the interference effect of the object on the rotor is primarily classified into three categories[15]: Ground Effect (GE), Lateral Wall Effect (LWE), and Ceiling Effect (CE).[16–18] Previous research has demonstrated that when the rotor of an aerial vehicle approaches the ground, the rotor wake is compelled to expand radially along the blade spanwise (radial) direction near the ground. Theoretically, these obstacles alter the velocity and orientation at the end of the wake and consequently beneficially affect the thrust and power requirements of the rotor.[19,20] To investigate the effect of the ground on rotor wake characteristics, Milluzzo et al.[21] employed a Particle Image Velocity (PIV) test system to analyze the wake characteristics of rotors with different tip shapes. The findings revealed that the tip shape exerts a significant influence on the rotor wake in the ground effect. Research has demonstrated that the ceiling effect affects the rotor inflow wake, reducing the pressure in the confined space between the rotor and the ceiling. The result of this phenomenon is that the local pressure on the upper surface of the rotor decreases, thereby increasing the rotor thrust and enhancing the rotor aerodynamic efficiency.[16,18,19] Conyers and Calomiris[22] has revealed that as the rotor approaches a wall, the wall affects the rotor inflow structure, reducing inflow in the local area of the rotor disc near the wall. This phenomenon leads to an asymmetric load distribution on the rotor disc, generating a moment that causes the aircraft to tilt towards the wall.

In addition, rotorcraft is susceptible to interference when approaching the water surface or crossing the air–water interface. Currently, Semenov[23] developed a study to investigate the influence of near-water-surface interference on rotor aerodynamic characteristics. In contrast to the ground effect, a moving rotor near the water surface experiences not only a weakened ground effect but also phenomena such as the inverse ground effect, which means the thrust decrease with the distance of the rotor and the water surface. Additionally, the rotor wake impacts the water surface, and the water waves caused by the downwash affect the diffusion of rotor wake, making the rotor flow field more complex. This phenomenon affects the rotor's aerodynamic characteristics, making it difficult to control the aircraft's attitude when it is near the water surface, further complicating the design of the control system. A study carried out by Mi[24] using CFD methods examined the variations in the aerodynamic characteristics of a duct fan operating near the water with and without waves. The research from Wang et al.[25] showed that the thrust of the duct fan reduces when there is water-surface interference, and the resulting thrust can be even less than that without ground interference. In general, the design of conventional rotorcraft operating from water involves increasing the height of aerodynamic components such as the rotor above the water surface to mitigate the impact of water splashes caused by the rotor wake on the aerodynamic performance. However, AAR is required to operate in close proximity to the water surface and to transition between air and water. Consequently, the proximity to the water surface inevitably affects the aerodynamic performance of the rotor.

Therefore, developing an aerodynamic model for a rotor operating in close proximity to a water surface poses a formidable challenge.[26] Previous research has explored various techniques to model the aerodynamics of the rotor in ground effect. Cheeseman and Bennett[27] employed a potential source in potential flow theory and image method to develop an aerodynamic model for the rotor in ground effect. Pulla[28] and Liang et al.[29] developed an aerodynamic model for the rotor in the ground effect based on lifting line and lifting surface theories. Mi,[24] Liu et al.,[30] Sugiura et al.[31] and Ji et al.,[32] utilized CFD methods to investigate the near-ground and near-surface aerodynamic characteristics of the rotor, leading to the development of numerical simulation models for the rotor in ground effect. The panel-vortex particle method has been used in the study of Tan et al.[33] to examine the impact of the ground on the rotor, presenting a numerical computational model for the rotor in ground effect. An aerodynamic prediction model for unmanned aerial vehicles based on neural networks was developed by Wang et al.[34] Research by Calomiris[22] presented a near-ground aerodynamic model for the rotor using the PFM method. Refs.[35–37] employed experiment methods to investigate the influence of the ground on the aerodynamic performance of unmanned aerial vehicles.

Therefore, the water surface has a significant influence on the rotor aerodynamic characteristics, and current research often overlooks the impact of near-surface interference.[15] Traditional numerical methods based on CFD struggle with the critical challenges of high computational cost, slow computational speed, and the propensity for divergence during cross-media two-phase flow calculations.[38] In the current study, Wang et al.[25] established an unsteady numerical simulation method suitable for AAR based on the volume of fluid method. In their results, they found that the presence of a flexible water surface played the role of a rotor rectifier, accelerating the dissipation of ground vortices and rotor tip vortices,

causing the distribution of the lift coefficient and torque coefficient of the rotor under the influence of the water surface to become more periodic and regular, and the water effect is not as strong as the foundation effect. However, this is an initial form of the gas–liquid flow field on the water surface. Zhao et al.[39] studied the hovering performance of ducted propellers at different heights above the water surface based on the lattice Boltzmann method. It was hypothesized the vortex ring state was the primary factor responsible for the observed instability, however, this conclusion was not wholly conclusive. Furthermore, the lack of systematic research on the interference mechanism of the gas–liquid flow field on the rotor aerodynamic characteristics imposes limitations on the structural and control system design of the AAR. Consequently, it is imperative to study the interference mechanism of surface water on rotor aerodynamic characteristics, develop a high-precision dynamics model, and provide a theoretical basis for the AAR design. The proposed aerodynamic model, which accounts for near-water-surface two-phase flow interference, can be utilized for initial performance evaluation and flight dynamics modeling.

The remainder of this paper is organized as follows. Firstly, an adaptive aerodynamic model considering the near-ground/near-water interference is proposed, which takes into account the deformation of the water surface. Furthermore, a near-ground/near-water rotor experimental system based on STM32 is constructed, and a series of experiments with different rotors are carried out to investigate the factors affecting the rotor aerodynamic performance. Finally, based on the experimental results and the fitting method, a transition boundary of the gas–liquid flow field stage is presented.

2. Methodology

2.1. Potential flow theory

The flow field is assumed as homogeneous, incompressible, and inviscid and the airflow is irrotational, except for the wake trailing from the trailing edge of the rotor, the relationship between the vorticity field and the flow field velocity can be expressed as

$$\boldsymbol{\omega} = \nabla \times \boldsymbol{u} \tag{1}$$

where $\boldsymbol{\omega}$ is the vorticity field, $\boldsymbol{u}$ is the velocity field, the vorticity field satisfies the solenoidal condition, which means $\nabla \cdot \boldsymbol{\omega} = 0$. In a Cartesian coordinate system (x, y, z), this relation yields the following relationships between the velocity components (u_x, u_y, u_z) and the vorticity components $(\omega_x, \omega_y, \omega_z)$.

Furthermore, a relationship based on the incompressible flow assumption can be obtained:

$$\begin{cases} \omega_x = \frac{\partial u_z}{\partial y} - \frac{\partial u_y}{\partial z} \\ \omega_y = \frac{\partial u_x}{\partial z} - \frac{\partial u_z}{\partial x} \\ \omega_z = \frac{\partial u_y}{\partial x} - \frac{\partial u_x}{\partial y} \end{cases} \tag{2}$$

Combining Eq. (1) and Eq. (2), a vector Poisson equation for the velocity$\boldsymbol{u}$ in terms of the vorticity [40] can be obtained:

$$\Delta \boldsymbol{u} = -\nabla \times \boldsymbol{\omega} \tag{3}$$

The circulation of the vorticity field around a closed curve L enclosing a surface S is defined as

$$\Gamma = \int_L \boldsymbol{u} \mathrm{d}\boldsymbol{\varepsilon} = \int_S \boldsymbol{\omega} \cdot \boldsymbol{n} \mathrm{d}S \tag{4}$$

where Γ is the circulation strength of the curve L, $\mathrm{d}\boldsymbol{\varepsilon}$ represents an element of the curve L, $\boldsymbol{n}$ is a unit normal of surface S.

In the flow field, there are multiple vortex filaments, one of which has a strength of Γ_0. The downwash velocity at an arbitrary point P in space induced by the vortex element $\mathrm{d}\boldsymbol{\varepsilon}$ of the vortex filament can be obtained from the Biot-Savart law. [40] Therefore, the solution of Eq. (3) is addressed as

$$\Delta \boldsymbol{u} = \frac{\boldsymbol{\lambda} \times \boldsymbol{\Gamma}_0}{4\pi |\boldsymbol{\lambda}|^3} \tag{5}$$

where $\boldsymbol{\Gamma}_0 = \Gamma \cdot \mathrm{d}\boldsymbol{\varepsilon}$ is the circulation strength of the vortex element $\mathrm{d}\boldsymbol{\varepsilon}$, and $\boldsymbol{\lambda}$ represents the vector from the vortex element to the point P.

2.2. Aerodynamic modeling

2.2.1. Finite vortex rotor model

In practice, the spanwise distribution of the profile of AAR rotors is variable, with the torsion angle, airfoil characteristics, and chord length varying along the blade radius. The tangential velocity of the rotor element linearly increases along the spanwise direction, which leads to a non-uniform distribution of the rotor circulation. The single vortex ring model has certain limitations in describing the three-dimensional rotor aerodynamic wake. For a more accurate description of the rotor model, a continuous Finite Vortex Rotor Model (FVRM) based on potential flow theory is presented. Inspired by the finite element method,[41] the rotor disc is treated as a plane with a radius of R, where the plane is discretized into a finite number of vortex ring filaments as illustrated in Fig. 1. The circulation strength of the kth vortex ring filament is Γ_k. There are an infinite number of vortex elements settled on the filament, and the circulation of each vortex element of a length of $d\boldsymbol{\varepsilon}$ can be expressed as

$$\boldsymbol{\Gamma}_\varepsilon = \Gamma_k \mathrm{d}\boldsymbol{\varepsilon} = \Gamma_k [-\sin\psi, \cos\psi, 0] r \mathrm{d}\psi \tag{6}$$

where $\boldsymbol{\Gamma}_\varepsilon$ represents the strength and vector of the circulation of the vortex element $\mathrm{d}\boldsymbol{\varepsilon}$, ψ is the azimuth of the vortex element in the rotor plane, r is the radius of the vortex ring filament ($0 < r < R$). When the vortex element is small enough, the length of the vortex element $\mathrm{d}\boldsymbol{\varepsilon}$ can be substituted by the point $Q(x_0, y_0, z_0)$. The distance from an arbitrary point $P(x, y, z)$ to the point Q is represented by

$$\boldsymbol{\lambda} = Q - P = [x_0 - x, y_0 - y, z_0 - z] \tag{7}$$

In addition, the rotor is discretized into a series of segments along the radial direction, with each vortex segment having a length of $\mathrm{d}r$. In the rotor plane, it is assumed that the vorticity and wake vortices of rotor, trailed by the rotor segments, can be represented by the vortex ring filaments as shown in Fig. 1. Each rotor segment trails a vortex ring filament. Based on Eq. (5), the induced velocity of the point $P(x, y, z)$ induced by the element $\mathrm{d}\boldsymbol{\varepsilon}$ is obtained:

$$\mathrm{d}\boldsymbol{u} = \frac{\boldsymbol{\lambda} \times \boldsymbol{\Gamma}_\varepsilon}{4\pi |\boldsymbol{\lambda}|^3} \tag{8}$$

It is worth noticing that when the vortex filament is discretized into sufficiently small elements as small as enough, the vortex element can be treated as a point. However, when

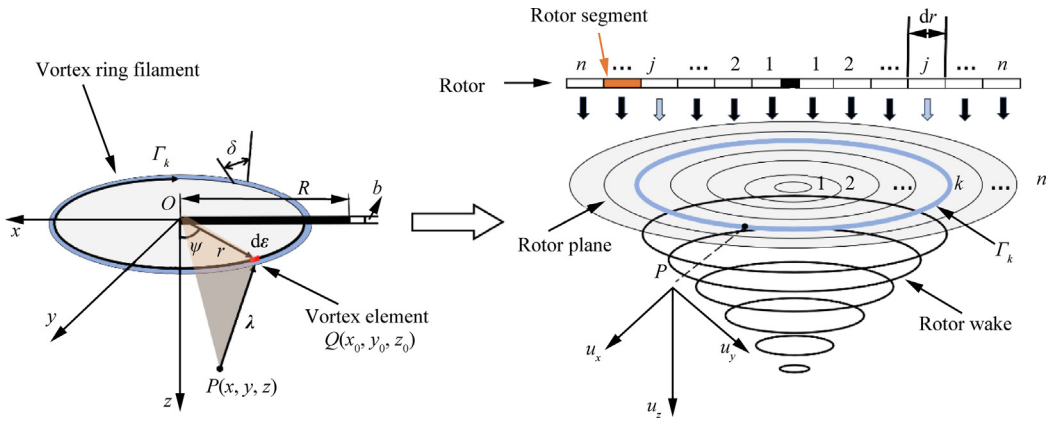

Fig. 1 Aerodynamic model based on finite vortex rotor model.

point P is located near the vortex ring filament, it can lead to singularity in the induced velocity. Therefore, the vortex core thickness δ is introduced to eliminate the singularity. Then, the projected induced velocity of the point P obtained from the Eq. (8) along the axial directions of the coordinate system are obtained,

$$\begin{cases} \mathrm{d}u_x = \frac{\Gamma_k r}{4\pi} \cdot \frac{z\cos\psi}{(|\lambda|^2+\delta^2)^{3/2}}\mathrm{d}\psi \\ \mathrm{d}u_y = \frac{\Gamma_k r}{4\pi} \cdot \frac{-z\sin\psi}{(|\lambda|^2+\delta^2)^{3/2}}\mathrm{d}\psi \\ \mathrm{d}u_z = \frac{\Gamma_k r}{4\pi} \cdot \frac{(x_0-x)\cos\psi+(y_0-y)\sin\psi}{(|\lambda|^2+\delta^2)^{3/2}}\mathrm{d}\psi \end{cases} \tag{9}$$

where u_x is the radial component of the induced velocity of the point P, u_y is the tangential component of the induced velocity, u_z is the axial (vertical) component of the induced velocity, $|\boldsymbol{\lambda}|^2 = (x_0 - x)^2 + (y_0 - y)^2 + (z_0 - z)^2$.

In this research, when considering the hovering state, it is assumed that the velocity of the vehicle is equal to zero. Based on this, it can be observed that the rotor plane is a symmetric about the plane O_{PQ} formed by the points P and Q, which means the plane O_{PQ} can be assumed as the initial coordinate plane. Therefore, the position of the point P is expressed as P (x, 0, z). The position of the vortex element is expressed as $x_0 = r\cos\psi$, $y_0 = r\sin\psi$, $z_0 = 0$. Then, the distance between the point P and vortex element can be expressed as

$$|\boldsymbol{\lambda}|^2 = r^2(1 + \bar{x}^2 + \bar{z}^2 - 2\,\bar{x}\cos\psi) \tag{10}$$

where $\bar{x} = x/r$, $\bar{z} = z/r$, and combining the Eq. (9), the axial (vertical) component of the rotor induced velocity is rewritten as

$$\mathrm{d}u_z = \frac{\Gamma_k}{4\pi r} \cdot \frac{1 - \bar{x}\cos\psi}{(1 + \bar{x}^2 + \delta^2 + \bar{z}^2 - 2\bar{x}\cos\psi)^{3/2}}\mathrm{d}\psi \tag{11}$$

Considering the entire vortex ring filament, the induced velocity of the point P is integrated along the vortex filament. It is expressed as

$$u_z = \frac{\Gamma_k}{4\pi r}\int_0^{2\pi} \frac{1 - \bar{x}\cos\psi}{(1 + \bar{x}^2 + \delta^2 + \bar{z}^2 - 2\bar{x}\cos\psi)^{3/2}}\mathrm{d}\psi \tag{12}$$

Eq. (12) can be rewritten by the first substitution of $\psi = 2\theta$, which becomes

$$u_z = \frac{\Gamma_k}{2\pi r}\int_0^{\pi} \frac{1 + \bar{x} - 2\bar{x}\cos^2\theta}{(1 + \bar{x}^2 + \delta^2 + \bar{z}^2 + 2\bar{x} - 4\bar{x}\cos^2\theta)^{3/2}}\mathrm{d}\theta \tag{13}$$

Eq. (13) can be rewritten by the second substitution of $\theta = \pi/2 - \phi$, which can be rearranged as

$$u_z = \frac{\Gamma_k}{2\pi r}\int_{-\pi/2}^{\pi/2} \frac{1 + \bar{x} - 2\bar{x}\sin^2\phi}{(1 + \bar{x}^2 + 2\bar{x} + \delta^2 + \bar{z}^2 - 4\bar{x}\sin^2\phi)^{3/2}}\mathrm{d}\phi \tag{14}$$

Substituting with $\kappa = (1 + \bar{x})^2 + \bar{z}^2 + \delta^2$, the Eq. (14) can be written as

$$u_z = \frac{\Gamma_k}{\pi r\kappa^{3/2}}\int_0^{\pi/2} \frac{1 + \bar{x} - 2\bar{x}\sin^2\phi}{(1 - \sigma^2\sin^2\phi)^{3/2}}\mathrm{d}\phi \tag{15}$$

where $\sigma^2 = 4\bar{x}/\kappa$. For convenience of calculation, Eq. (15) can be rewritten as follows:

$$u_z = \frac{\Gamma_k}{\pi r\kappa^{3/2}}\left[\int_0^{\pi/2} \frac{1+\bar{x}}{(1-\sigma^2\sin^2\phi)^{3/2}}\mathrm{d}\phi - \int_0^{\pi/2} \frac{2\bar{x}\sin^2\phi}{(1-\sigma^2\sin^2\phi)^{3/2}}\mathrm{d}\phi\right] \tag{16}$$

Introducing the first kind of incomplete elliptic integral K and the second kind of elliptic integral E, which are

$$K = \int_0^{\pi/2} \frac{1}{\sqrt{1 - \sigma^2\sin^2\phi}}\mathrm{d}\phi$$

$$E = \int_0^{\pi/2} \sqrt{1 - \sigma^2\sin^2\phi}\mathrm{d}\phi$$

$$D = \int_0^{\pi/2} \frac{\sin^2\phi}{\sqrt{1 - \sigma^2\sin^2\phi}}\mathrm{d}\phi = \frac{K - E}{\sigma^2}$$

Alternatively, by simplifying Eq. (16), an equivalent result can be expressed as follow:

$$u_z = \frac{\Gamma_k}{\pi r\kappa^{3/2}}\left[(1 + \bar{x})\frac{E}{1 - \sigma^2} - 2\,\bar{x}\,\frac{K - D}{1 - \sigma^2}\right] \tag{17}$$

When the AAR keep in the hovering condition, the rotor circulation strength is symmetrically distributed about the plane O_{PQ}. The integration of the tangential induced velocity for the whole vortex filament acting on the point P cancels out, which means $u_y = 0$. Consequently, the radial component of induced velocity can be expressed as

$$u_x = \frac{\Gamma_k}{\pi r \kappa^{3/2}} \left(2\bar{z}\,\frac{K-D}{1-\sigma^2} - \bar{z}\,\frac{E}{1-\sigma^2} \right) \tag{18}$$

A special case when the point P is located at the center of the rotor plane, which means $z = 0$, $x = 0$ and $\sigma = 0$. The induced velocity generated by the k vortex ring filament is addressed as

$$u_{z,k}^{\text{center}} = \frac{\Gamma_k}{\pi r} E = \frac{\Gamma_k}{2r} \tag{19}$$

Correspondingly, the presence of each vortex ring filament will result in an axial velocity. Therefore, the induced velocity of the segment j ($j = 1, 2, \ldots, n$) should be expressed as the superposition of all vortex ring filaments, which is

$$v_z^j = u_{z,1}^j + \ldots + u_{z,k}^j + \ldots + u_{z,n}^j \tag{20}$$

where v_z^j is the axial (vertical) component of the induced velocity of the rotor segment j, and $u_{z,k}^j$ is the axial velocity of the segment j induced by the vortex ring filament k. Moreover, the axial induced velocity distribution of the rotor disc can be expressed as $\boldsymbol{V}^{\text{full}}$. Especially, the axial induced velocity at the rotor disc center can be derived from the Eq. (19). Therefore, the full induced velocity distribution on the rotor plane is

$$\boldsymbol{V}^{\text{full}} = [v_z^n, \ldots, v_z^2, v_z^1, v_z^{\text{center}}, v_z^1, v_z^2, \ldots, v_z^n] \tag{21}$$

Based on the momentum theory, the thrust generated by a rotor segment dr is defined as

$$\mathrm{d}T_j = 2\rho (v_z)^2 b \mathrm{d}r \tag{22}$$

where b is the chord length of the rotor segment, ρ is the ambient density, v_z is the axial component of the induced velocity of the rotor segment, $\mathrm{d}T_j$ is the thrust of the rotor segment k. The thrust of the rotor disc is obtained by integrating the thrust of the rotor segment along the radial direction.

When the rotor circulation is uniformly distributed, the aerodynamic performance is optimal with minimum induced power. This means that the circulation distribution is

$$\boldsymbol{\Gamma}_m = [\Gamma_1, \Gamma_2, \ldots, \Gamma_n] \tag{23}$$

However, the rotor circulation is never uniformly distributed along the radial direction. In this paper, three distribution models are considered, which are defined as

$$\boldsymbol{\Gamma}_m = \begin{cases} \Gamma_k = \Gamma_u, & \text{Uniform} \\ \Gamma_k = \Gamma_u r, & \text{Linear} \\ \Gamma_k = \Gamma_u r^2, & \text{Quadratic} \end{cases} \tag{24}$$

where $k = 1, 2, \ldots, n$. Γ_u represents the circulation strength of the rotor segment in the blade root, $\boldsymbol{\Gamma}_m$ is the circulation matrix.

To account for the influence of the ground plane on the rotor wake, the distance between the rotor and the ground plane is defined as h. Following the image method, the real rotor and the image rotor are symmetrically positioned about the ground plane, with the image rotor located at twice the rotor-to-ground distance ($2h$). The image method can be used to modify the induced velocity of the rotor segment j, as shown in Fig. 2. For the rotor segment j, the vertical component of the induced velocity is expressed as

$$v_{\text{IGE}}^j = v_{\text{OGE}}^j - \Delta v^j \tag{25}$$

where Δv^j represents the velocity increment of the rotor segment j induced by the rotor image model, v_{OGE}^j is the velocity of the segment j without the ground effect (Out of the Ground Effect, OGE), v_{IGE}^j is the velocity of the segment j in the ground effect (In the Ground Effect, IGE). It is assumed that the circulation strength of the image model is equal to the rotor's circulation without the ground effect, due to the symmetrical distribution. The influence of the image model on the induced velocity can be expressed as

$$\Delta v^j = \sum_{k=1}^{n} w_k^j = \sum_{k=1}^{n} \frac{\Gamma_{k,\text{image}}}{\pi r \kappa^{3/2}} \left[(1+\bar{x})\,\frac{E}{1-\sigma^2} - 2\bar{x}\,\frac{K-D}{1-\sigma^2} \right] \tag{26}$$

where w_k^j is the velocity of rotor segment j induced by the vortex ring filament k of the image model with the circulation strength of $\Gamma_{k,\text{image}}$. Then, the induced velocity distribution of the rotor is obtained as

$$\boldsymbol{V}_{\text{IGE}}^{\text{full}} = [v_{\text{IGE}}^n, \ldots, v_{\text{IGE}}^2, v_{\text{IGE}}^1, v_{\text{IGE}}^{\text{center}}, \ldots, v_{\text{IGE}}^1, v_{\text{IGE}}^2, \ldots, v_{\text{IGE}}^n] \tag{27}$$

where $\boldsymbol{V}_{\text{IGE}}^{\text{full}}$ is the induced distribution of the whole rotor disc. Finally, the estimated thrust in the ground effect is calculated by integrating the induced velocity distribution along the rotor radius, according to Eq. (22).

2.2.2. Model modification strategy

In this subsection, an aerodynamic modification strategy that accounts for the aerodynamic interference of the rotor near the water surface is presented. The focus and challenge in modeling the rotor-near-water-surface aerodynamic model rely on modifying the aerodynamic interference caused by the coupling between the water surface and the rotor flow field. When the aircraft rotor approaches the water surface, the flexible water surface deforms under the impact of the downwash, as shown in Fig. 3(a). This phenomenon causes irregular fluctuations in the rotor thrust. However, previous studies have only considered the effect of ground impact on the rotor aerodynamic model.

In the experimental process, as illustrated in Fig. 3(a), it can be observed that the water surface gradually declines under the impact of the rotor downwash, with the deformation becoming more pronounced as it approaches the center of the rotor. Simultaneously, a significant number of droplets are generated from the edges of these depressions, dispersing outwards under the influence of the airflow impact and rotor wake vortexes. Therefore, the rotor airflow field disturbed by the water surface is simplified into a model as shown in Fig. 3(b). To derive the relationship between the water surface interference factors and the rotor flow field, the following assumptions are made:

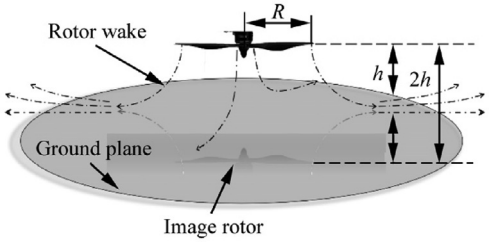

Fig. 2 Rotor aerodynamic interference model based on image method.

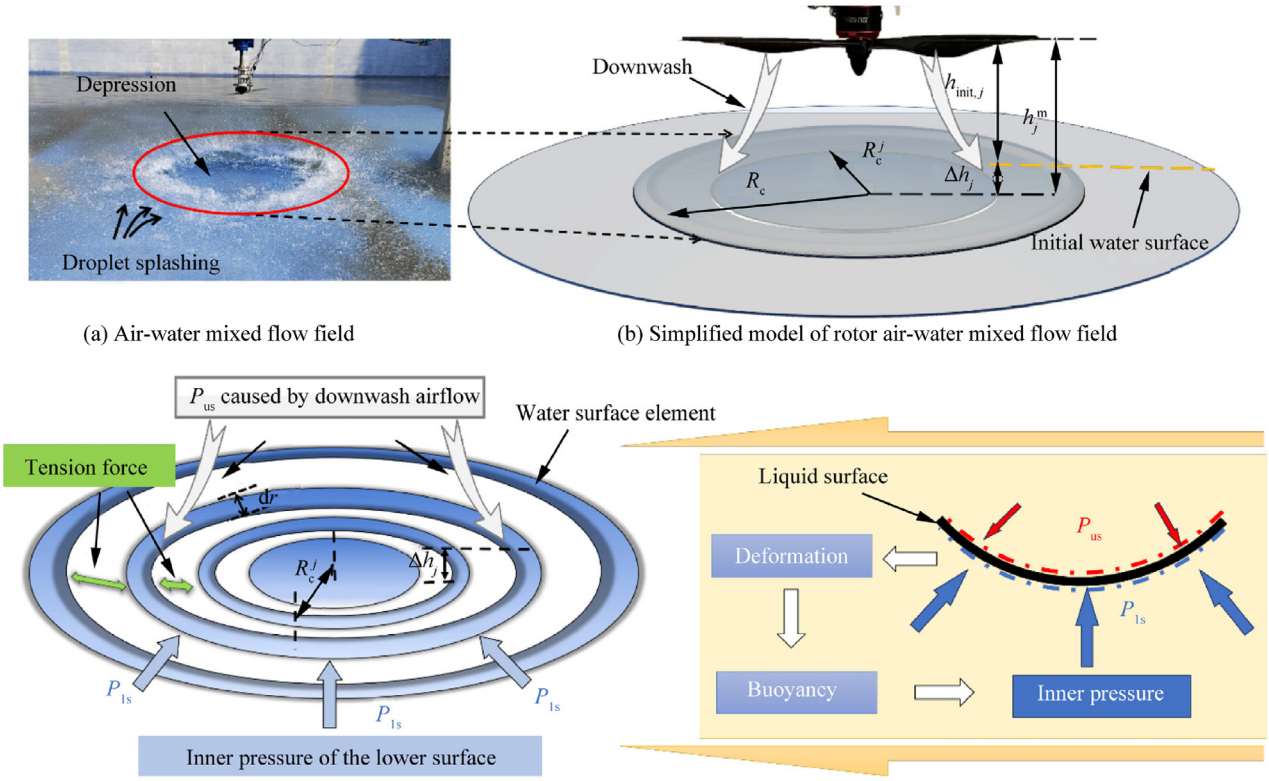

Fig. 3 Hypothetical similarity model of water surface.

Assumption 1. The fluid flows slowly due to the viscosity and the shear effect of the wall jet. Therefore, in order to reduce the complexity of the model, an energy conservation assumption has been employed and the rotor wake is assumed to expand without energy exchange as it spreads along the water surface.

Assumption 2. The depth of the depression depends mainly on the momentum of the rotor downwash. Therefore, the deformed area of the water surface is conceptualized as a regular sink that changes uniformly from the center of the depression to the surrounding area. Thus, it is assumed that the impulse increment on the upper surface of the water surface can be equivalent to the momentum loss of the rotor downwash.

Assumption 3. It is assumed that the deformation of the water surface generates a buoyancy exerted on the lower surface of the deformation area like an immersed object.

In the research presented by Hwang et al.[42,43] the surface deformation caused by the rotor downwash is described as a depression, whose depth and curvature vary with the radial distance. Research has found that the depth variation of the water surface depression is governed by the initial rotor height h and the downwash velocity reaching water surface. Subsequently, the water surface is radially discretized into a series of ring elements with a width dr, where the discretization resolution matches the number of rotor segments, as shown in Fig. 3(c). Therefore, the actual rotor height of each rotor segment should be expressed as the superposition of initial height and the water deformation. Then, the modified height of each rotor segment should be expressed as

$$h_j^{\text{m}} = h_{\text{init},j} + \Delta h_j \tag{28}$$

where Δh_j is the height increment of the rotor segment, $h_{\text{init},j}$ is the initial rotor height between the rotor plane and water surface, h_j^{m} is the modified height of the rotor segment j.

In Eq. (28), according to the research of Qian et al. [44] the distribution of the depth of the water depression is also related to the surface tension of the liquid. In addition, the research has also shown that the viscosity of the liquid has no significant effect on the changes in the depth of depression. Therefore, the approximate model for the depth of the water depression is obtained as

$$\Delta h = g(\mu_{\text{imp}}, h, \sigma_w) \tag{29}$$

where μ_{imp} is the effective impinging velocity of the downwash reaching water surface, and σ_w is the surface tension coefficient of the liquid. The liquid surface is compressed and deformed under the action of the rotor downwash.

The pressure of the upper liquid surface (P_{us}) and the equilibrium force exerted on the water surface (F_{us}) can be expressed as

$$F_{\text{us}} = \int_0^{A_{\text{d}}} P_{\text{us}} \text{d}s \tag{30}$$

where P_{us} is the pressure distribution in the upper liquid surface under the impinging of the wake downwash, A_{d} is the area

of the water depression zone, and the ds is the unit area of the deformation region. It is assumed that the depression is hemispherical, the surface area can be approximated by $A_{\mathrm{d}} = 2\pi R_{\mathrm{c}}^2 \approx 2\pi R^2$, where R_{c} is the curvature radius of the water depression zone.

Since the rotor is very close to the water surface, the downwash velocity reaching the liquid surface can be approximated as the induced velocity in the rotor plane, which means $\mu_{\mathrm{imp}} = -v_z$. Based on the conservation of momentum theorem, the momentum of the rotor downwash reaching the water surface is equal to the momentum of the airflow through the rotor plane. Therefore, the impact force can be expressed as

$$F_{\mathrm{imp}} = \dot{m}\, u_{\mathrm{imp}} = \dot{m}\, v_z = \rho_{\mathrm{a}} S_R (v_z)^2 \tag{31}$$

where S_R is the area of the rotor disc, $S_R = \pi R^2$, F_{imp} is the impinging force of the downwash, ρ_{a} is the air density, $\dot{m}$ is the mass flow in the rotor plane, v_z is axial component of the induced velocity.

It is assumed that there is no energy dissipation and loss in the process of energy exchange between the rotor downwash and the water surface, which means that the deformation of the water absorbs all the momentum of downwash. Then, the pressure distribution on the water surface can be obtained as

$$P_{\mathrm{us}} = F_{\mathrm{us}}/A_{\mathrm{d}} = F_{\mathrm{imp}}/A_{\mathrm{d}} \tag{32}$$

According to Young-Laplace Law,[45,46] when the liquid surface achieved a short-term dynamic equilibrium under the effect of the external force and the liquid surface tension. Furthermore, the water surface was divided into a finite number of elements as shown in Fig. 3(c). The upper surface of each element is subjected to the momentum caused by the rotor downwash. The lower surface generates a pressure increment due to the descent of the liquid surface, which can be obtained based on the principle of buoyancy. The pressure of the lower surface of the depression area can be approximated by $\rho_w g \Delta h_j$. The edge of the element is influenced by the surface tension from the adjacent elements, which can be obtained from the tension coefficient σ_w. Then, the equilibrium equation for the deformation region with a width of dr, can be expressed as

$$\Delta P_{\mathrm{us}} - \Delta P_{\mathrm{ls}} = \frac{1}{2}\rho_{\mathrm{a}} v_z^2 - \rho_w g \Delta h_j = \frac{2\sigma_w}{R_{\mathrm{c}}^j} \tag{33}$$

where P_{ls} is the pressure of the lower liquid surface caused by the depression in the of the deformation area, g is acceleration due to gravity, ρ_w is the liquid density, R_{c}^j is the curvature radius of the water surface element. As reported in the Refs. 43,47, the curvature radius R_{c} of the depression region is defined as

$$R_{\mathrm{c}} = \frac{K_\alpha}{4(\Delta h_j)h^2} \tag{34}$$

where K_α is a constant determined by empirical coefficient. Furthermore, for a water depression zone of width dr, combining Eq. (33) and Eq. (34), the depth variation can be obtained as

$$\Delta h_j = \frac{\varepsilon}{h^2 + \zeta}(v_z^j)^2 \tag{35}$$

where $\varepsilon = K_\alpha \rho_{\mathrm{a}}/16\sigma_w$ and $\zeta = \rho_w g K_\alpha/8\sigma_w$. Then, the induced velocity under the influence of water surface can be obtained based on the FVRM as

$$\begin{aligned}\Delta v_m^j &= \sum_{k=1}^{n} w_k^j \\ &= \sum_{k=1}^{m} \frac{\Gamma_{k,\mathrm{image}}}{\pi r \kappa_m^{3/2}}\left[(1+\bar{x})\frac{E}{1-\sigma_m^2} - 2\bar{x}\,\frac{K-D}{1-\sigma_m^2}\right]\end{aligned} \tag{36}$$

where Δv_m^j (m is the first letter of modified) is the velocity increment induced by the image model under the interference of water surface of the rotor element j, and κ_m, σ_m represents the modified parameters value. Combining the Eq. (25), the full induced velocity distribution of the rotor is modified as

$$\boldsymbol{V}_{\mathrm{IWS}}^{\mathrm{full}} = [v_{\mathrm{IWS}}^n, \ldots, v_{\mathrm{IWS}}^2, v_{\mathrm{IWS}}^1, v_{\mathrm{IWS}}^{\mathrm{center}}, v_{\mathrm{IWS}}^1, v_{\mathrm{IWS}}^2, \ldots, v_{\mathrm{IWS}}^n] \tag{37}$$

where $\boldsymbol{V}_{\mathrm{IWS}}^{\mathrm{full}}$ is the induced velocity distribution in the Interference of Water Surface (IWS), the thrust of the rotor can be obtained based on Eq. (22).

2.2.3. Model adaptive method

In this subsection, an adaptive method is used to modify the circulation distribution to effectively account for the circulation variations and improve the computational efficiency. The thrust estimation process for the rotor considering the interference caused by water-surface is illustrated schematically in Fig. 4.

As shown in Fig. 4, in order to estimate the circulation accurately, the current circulation in each iteration is defined as

$$\boldsymbol{\Gamma}^{i+1} = \boldsymbol{\Gamma}^i + \Delta\boldsymbol{\Gamma} \tag{38}$$

where $\Delta\boldsymbol{\Gamma}$ is the circulation distribution increment which can be calculated from the coefficient matrix $\boldsymbol{A}$. The matrix is determined by the circulation distribution. The increment is expressed as,

$$\Delta\boldsymbol{\Gamma} = \boldsymbol{A}(\Gamma) e_T \tag{39}$$

where e_T is the error between the input data T_{input} and the calculation result T_{Est}.

$$e_T = T_{\mathrm{Est}} - T_{\mathrm{input}} \tag{40}$$

Finally, the main calculating procedure workflow is defined as follow:

(1) Input experiment data T_{OGE} as the initial data. Initializing the model parameters, such as the circulation distribution (Γ_1, Γ_2, …, Γ_n) and the induced velocity distribution $\boldsymbol{V}_{\mathrm{OGE}}^{\mathrm{full}}$.
(2) Updating the prediction thrust T_{Est}, calculating the estimation error e_T.
(3) If $e_T > 0.001$, updating the circulation distribution $\boldsymbol{\Gamma}_m$ (Γ_1, Γ_2, …, Γ_n) and backing to Step (2) until the error meets the requirements. Then, output the final results $\boldsymbol{\Gamma}_m$ (Γ_1, Γ_2, …, Γ_n) and $\boldsymbol{V}_{\mathrm{OGE}}^{\mathrm{full}}$.
(4) Initializing the image rotor model $\boldsymbol{\Gamma}_{m,\mathrm{image}}$ (Γ_1, Γ_2, …, Γ_n)$_{\mathrm{image}}$, updating the image induced velocity $\boldsymbol{V}_{\mathrm{IWS}}^{\mathrm{full}}$ and generating the rotor-ground/water height matrix $\boldsymbol{h}_{\mathrm{init}}$, ($\boldsymbol{h}_{\mathrm{init}} = [h_{\mathrm{init},1}, h_{\mathrm{init},2}, \ldots, h_{\mathrm{init},n}]$).
(5) Updating the height h_m^j and the induced velocity Δv_m^j. Then, iterating until the variation between the current $\Delta v_m^j(i+1)$ and the previous $\Delta v_m^j(i)$ is less than 10^{-4}.
(6) Output the rotor thrust T_{IGE} and T_{IWS}.

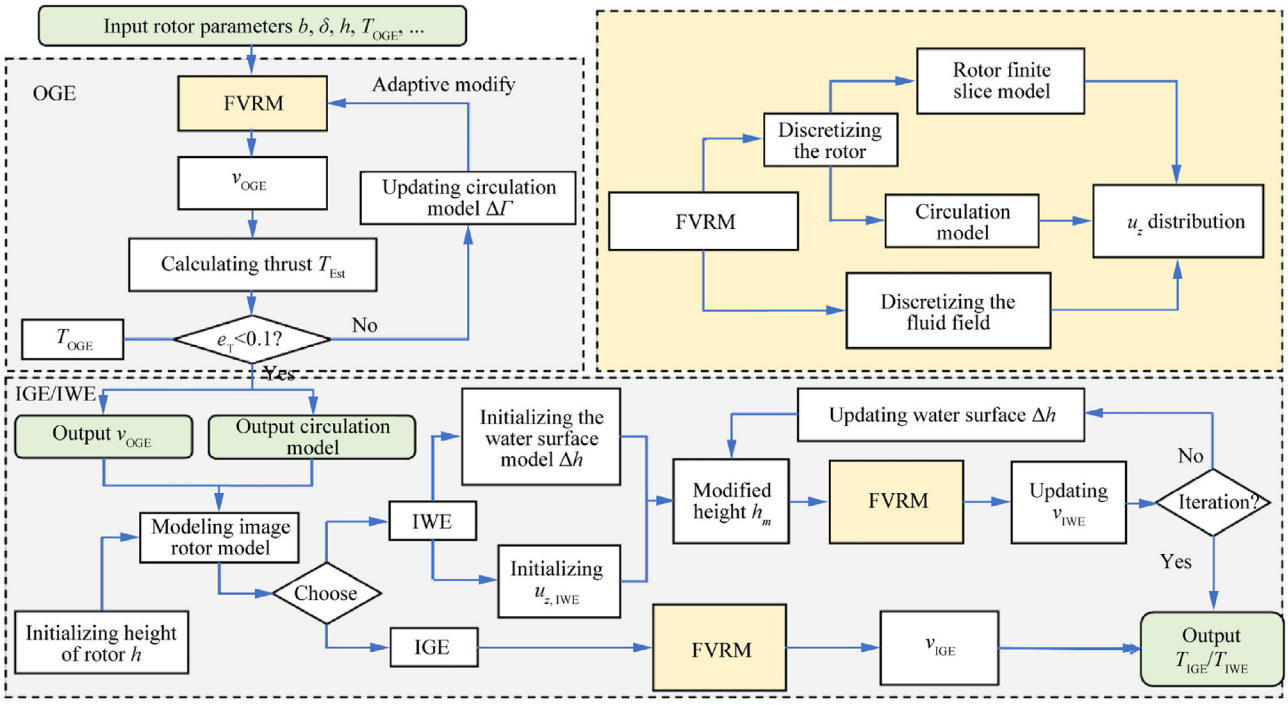

Fig. 4 Calculating procedure of rotor thrust based on FVRM model.

3. Results and discussion

In this section, an experimental setup is constructed to explore the interference factors exerted by the water surface on the rotor flow field. The parameters of the FVRM model are compared and optimized. Different aerodynamic models are compared to validate the performance of the FVRM model. Finally, based on the fitting method, a transition boundary for the flight safety zone is proposed.

3.1. Experiment system construction and analysis

The rotor experimental system depicted in Fig. 5 is constructed utilizing embedded development tools such as STM32. The experimental setup includes the rotor system, the data acquisition system, and the control system. The rotor system consists a regulated DC power supply, an ESC (Electronic Speed Controller), a brushless DC motor, and the rotor itself. The data acquisition system includes a force sensor (model DYLY-103), a torque sensor (model DYLN-101), a Hall-effect sensor (model A3144), and a voltage-current sensor (model INA226). The control system is built around an STM32 microcontroller, together with a stepper motor, digital stepper driver and encoder. A host computer is built based on the STM32 microcontroller. As shown in Fig. 5, the host computer adjusts the height of the rotor to the water surface by controlling the step angle of the stepper motor through the digital stepper driver, with closed-loop control of the step angle achieved via the encoder.

In actual engineering applications, a nearly constant speed is set in the helicopter rotor during the flight process, which means that the speed is directly related to the rotor power. Unlike helicopters, drones employ PWM (pulse width modulation) pulse signals to control the output power and speed of each motor, which is directly related to the rotor power and thrust. Therefore, in this research the motor electric power is introduced instead of the rotor power to survey the mapping between PWM duty cycle and rotor thrust, which is a more intuitive and meaningful approach compared to examining the relationship between rotor speed (rotor power) and rotor thrust. Consequently, the electronic speed control throttle value (ESC_T) is defined as the ratio of the current pulse width modulation duty input value (PD_{input}) to the PWM duty cycle range, which is expressed as

$$ESC_T = \frac{PD_{input}}{PD_{max} - PD_{min}} \times 100\% \tag{41}$$

During the experiment, some valuable phenomena and important conclusions were obtained. The research serves the design of a prototype with a take-off weight of 2 kg and equipped with a 0.24 m rotor. The rotor was used as the test object in order to ensure its loading capacity and to leave a certain amount of redundancy in the maneuvering power. In order to ensure the observability of the experiment while preventing the backflow of water from the wall and the interference of the wall on the rotor, a water tank was constructed with a length of 2 m, a width of 2 m, and a depth of 2 m. Then, Fig. 6 was taken at $h/R = 2$, and Fig. 7 was taken at $h/R = 0.8$.

Through the experiment, a number of phenomena were found, which are:

Phenomenon 1. At a low throttle phase, as shown in Fig. 6 when $0\% < ESC_T < 50\%$ and Fig. 7 when $0\% < ESC_T < 30\%$, the liquid surface descends due to the rotor downwash without droplet formation. At this phase, the effect of the liquid surface on the rotor is similar to the tra-

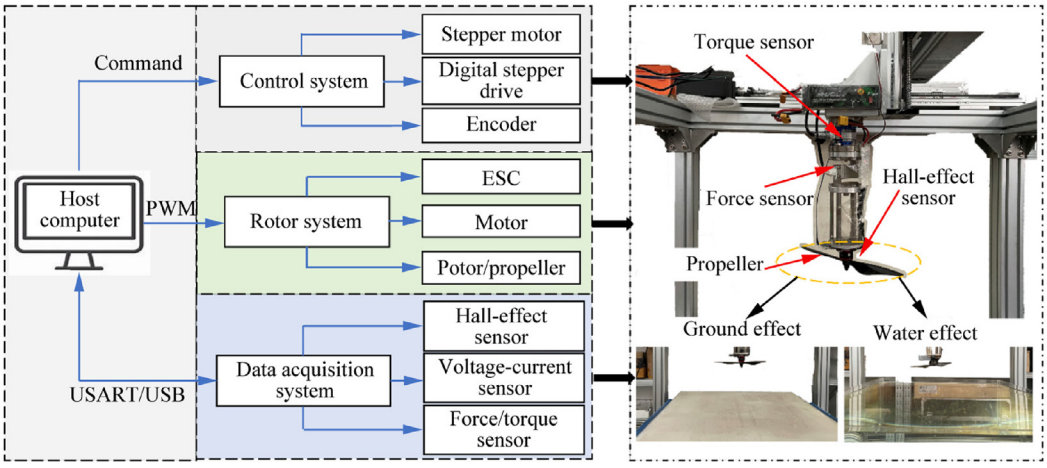

Fig. 5 Experiment system component diagram.

ditional ground effect. The rotor wake, which expands along the rotor axis, results in a change in orientation from axial flow to radial flow upon impact with the liquid surface. However, the radial airflow is compressed by the shedding tip vortex, resulting in the emergence of a wall jet close to the water surface. Therefore, it can be assumed that the main reason for the weakening of the rotor thrust increase is that the liquid surface descends under the effect of the rotor downwash.

Phenomenon 2. At a medium throttle phase, as shown in Fig. 6 when 60% < ESC_T and in Fig. 7 when 40% < ESC_T < 60%, the water surface exhibits a pronounced depression, accompanied by the generation of a minor quantity of droplets at the edge of the depressed zone and splashing outward along the radial direction of the rotor disc. At this phase, the liquid surface is deformed by the extrusion of the downwash flow, creating a liquid crown at the boundary of the deformation area. The liquid crown was broken by the shear effect of the wall jet, resulting in the formation of droplets. The minor droplets were uplifted with the upwelling induced by the shedding tip vortex and splashing outward. At this moment, the rotor thrust has a weakened positive gain effect under the influence of the water surface. The effect of this phenomenon on the aerodynamic performance of the rotor is still similar to a weak ground effect. Therefore, it can be attributed that the depressed liquid surface was the primary factor contributing to the weakening of the rotor thrust, which is equivalent to an increase in the distance between the rotor and the water surface.

Phenomenon 3. At a high throttle phase about 70% < ESC_T, as illustrated in Fig. 7, the gas–liquid flow field fluctuates under the interference of the rotor downwash and the water surface, which results in a series of phenomena include

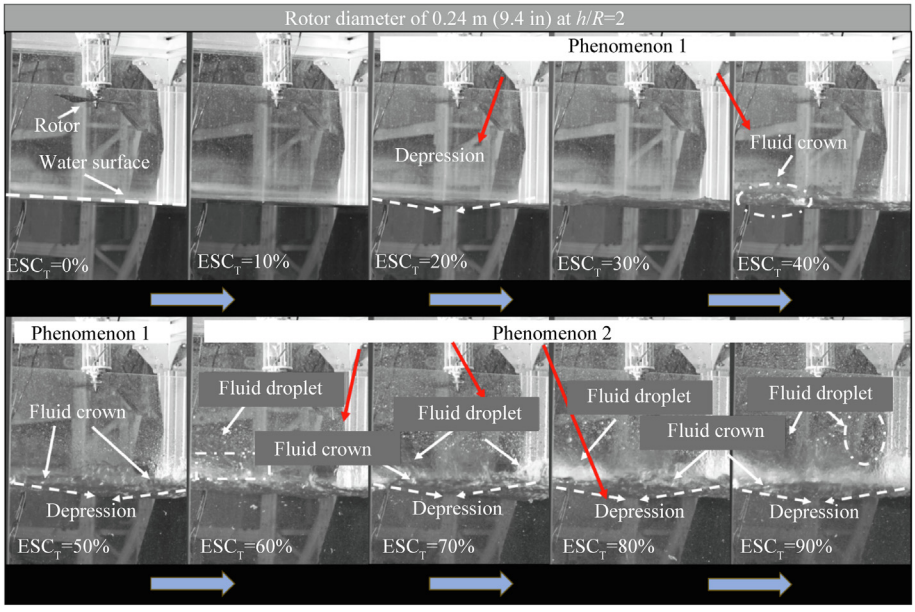

Fig. 6 Evolution process of gas–liquid flow field at $h/R = 2$.

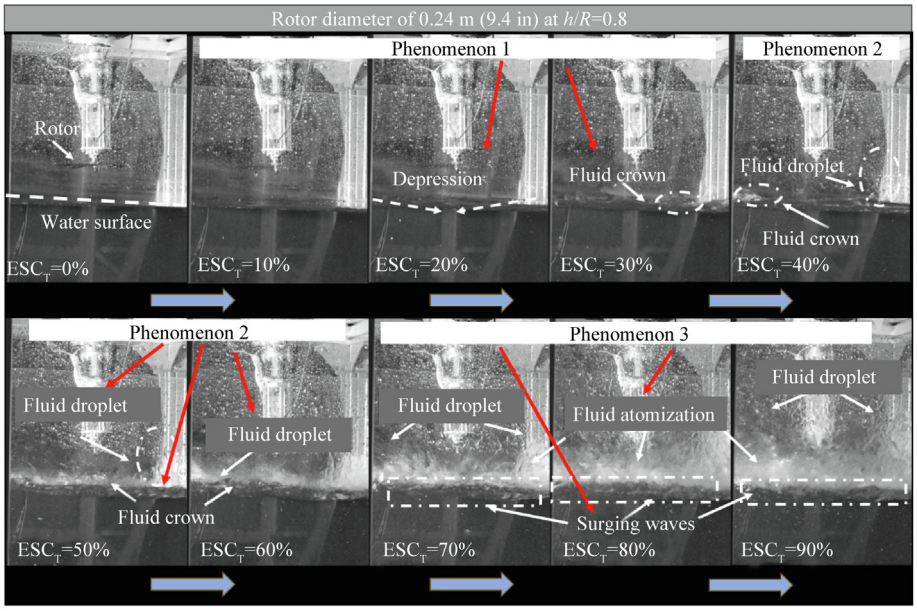

Fig. 7 Evolution process of gas–liquid flow field at $h/R = 0.8$.

surging wave, uplifted droplets, atomized droplets and sharp noise. Concurrently, the gas–liquid flow field make it a challenge to maintain a stable rotational speed or thrust. At this phase, the thrust reduces under the influence of the water surface, even to a level that is less than the thrust out of the ground effect. A significant number of smaller sized droplets collided with each other and were subsequently conveyed into the rotor plane, where they collided with the rotor. This resulted in atomization, which can be observed in Fig. 7 when $\mathrm{ESC_T} = 70\%$.

To further explore the reason of these phenomena, six sizes of the rotor were used in both near-ground and near-water experiments. Detailed parameters of each rotor are listed in Table 1. The blade pitch is defined as the distance that the rotor advances forward in one revolution.

In the experiment, it is observed that the sudden drop in rotor lift is due to the coupling of various interference factors. Factors such as rotor size, airflow rate per unit time through the rotor disc, mass flow rate per unit time, downwash velocity, motor throttle level (rotor required power), and rotor-water distance all affect the aerodynamic performance of the rotor near the water surface. In this section, we explore the effects of altering rotor size, rotor-water distance, and controlling motor throttle to adjust the airflow rate, mass flow rate, and downwash speed through the rotor disc per unit time to investigate how the water surface influences the aerodynamic performance of the rotor near the liquid. Overall, the water surface's impact on rotor aerodynamic performance is variable, complex, multifactorial, and challenging to predict accurately. Therefore, to investigate the relationship between rotor aerodynamic performance, airflow mass rate, flow speed, and motor throttle level, and to quantify test results to facilitate qualitative analysis, we propose using Disc Loading (DL), a key variable related to airflow rate and speed per unit time. The rotor disc loading is defined as

$$\mathrm{DL} = E_\mathrm{T}/S_R = 2E_\mathrm{T}/\pi D^2 \tag{42}$$

Table 1 Parameters of rotors.

Diameter (m)	Blade pitch (m)	Rotor disc area (m^2)
0.13	0.118	0.013 27
0.2	0.114	0.032 37
0.24	0.127	0.045 24
0.3	0.14	0.073 06
0.35	0.14	0.099 54
0.38	0.14	0.113 41

where E_T is the thrust of rotors in the experiment, D is the diameter of rotors.

Multiple groups of rotor experiments were conducted for both near-ground and near-water, including variations in rotor height and $\mathrm{ESC_T}$ values. The range of rotor heights varied from $3R$ to $0.4R$, specifically at heights of $3R$, $2R$, $1.5R$, R, $0.8R$, $0.6R$ and $0.4R$. For each height, the $\mathrm{ESC_T}$ value was adjusted from 10% to 90% with a 10% increment per step. The sampling frequency during the tests was set at 0.1 Hz. For each fixed height and $\mathrm{ESC_T}$ level, data were collected over a period of 3 s and the average measurement taken as the result. Several repeated trials were performed to ensure accuracy.

Fig. 8 and Fig. 9 show the results of the rotor torque and the rotational speed under a fixed $\mathrm{ESC_T}$ condition, respectively. Fig. 8 compares the variation characteristics of the rotor torque under different h/R conditions, while Fig. 9 depicts the rotor rotational speed variation with h/R. Fig. 8 shows that when the rotor approaches the water surface, the rotor torque increases sharply as h/R decreases. Fig. 9 shows the variation of the rotational speed in the influence of gas–liquid mixing flow field, where the rotational speed rapidly declines as h/R decreases near the water surface. Combining Fig. 8 and

Fig. 9, it can be noticed that under a fixed ESC_T, the influence of the gas–liquid mixing flow field gradually intensifies as the h/R descends. The complex two-phase flow field makes it challenging for the rotor to maintain the initial speed, prompting the ESC to increase rotor torque in an attempt to stabilize rotor power. This is an operational feature of the ESC that supports the further analysis in this study.

Fig. 10 illustrates the variation of rotor electric power with h/R under a fixed ESC_T condition. The figure indicates that when ESC_T is held constant, the rotor electric power remains stable in both the near-ground and near-water tests. Conventional methods, such as fixed power or fixed thrust, become less effective in gas–liquid flow field, where complex flow fluctuations make it challenging to define a constant required power or rotor thrust. Therefore, the electric power was proposed as a reference to explore rotor aerodynamic characteristics.

Fig. 11 illustrates a comparison of the rotor thrust measured for the near-ground and near-water experiments. P.1 represents the lift range when phenomenon 1 occurs, P.2 represents the lift range when phenomenon 2 occurs, and P.3 represents the lift range when phenomenon 3 occurs. Figs. 11(a)–(c) show that the common feature of both water and ground interference is that the rotor thrust increases with decreasing rotor height. In this phase, the influence of water on the rotor thrust is similar to a weakened ground effect. However, as observed in Fig. 11(d)–(f), when the rotor is too close to the water and the DL exceeds a threshold, the influence of the water surface on the rotor thrust changes from positive to negative gain, as described below:

(1) In the experiment with a 0.24 m diameter rotor, Fig. 11 (d) shows the transition from positive to negative gain on the rotor thrust occurs when $ESC_T > 90\%$ and $h/R < 0.6$.
(2) In the experiment with an 0.2 m diameter rotor, Fig. 11 (e) shows that one of the transition points occurs when $ESC_T > 80\%$ and $h/R < 0.4$; another one occurs when $ESC_T > 90\%$ and $h/R < 0.6$.
(3) In the experiment with a 0.13 m diameter rotor, several transition points can be identified in Fig. 11(f). The first point occurs when $ESC_T > 20\%$ and $h/R < 0.6$; The second point occurs when $ESC_T > 30\%$ and $h/R < 1$;

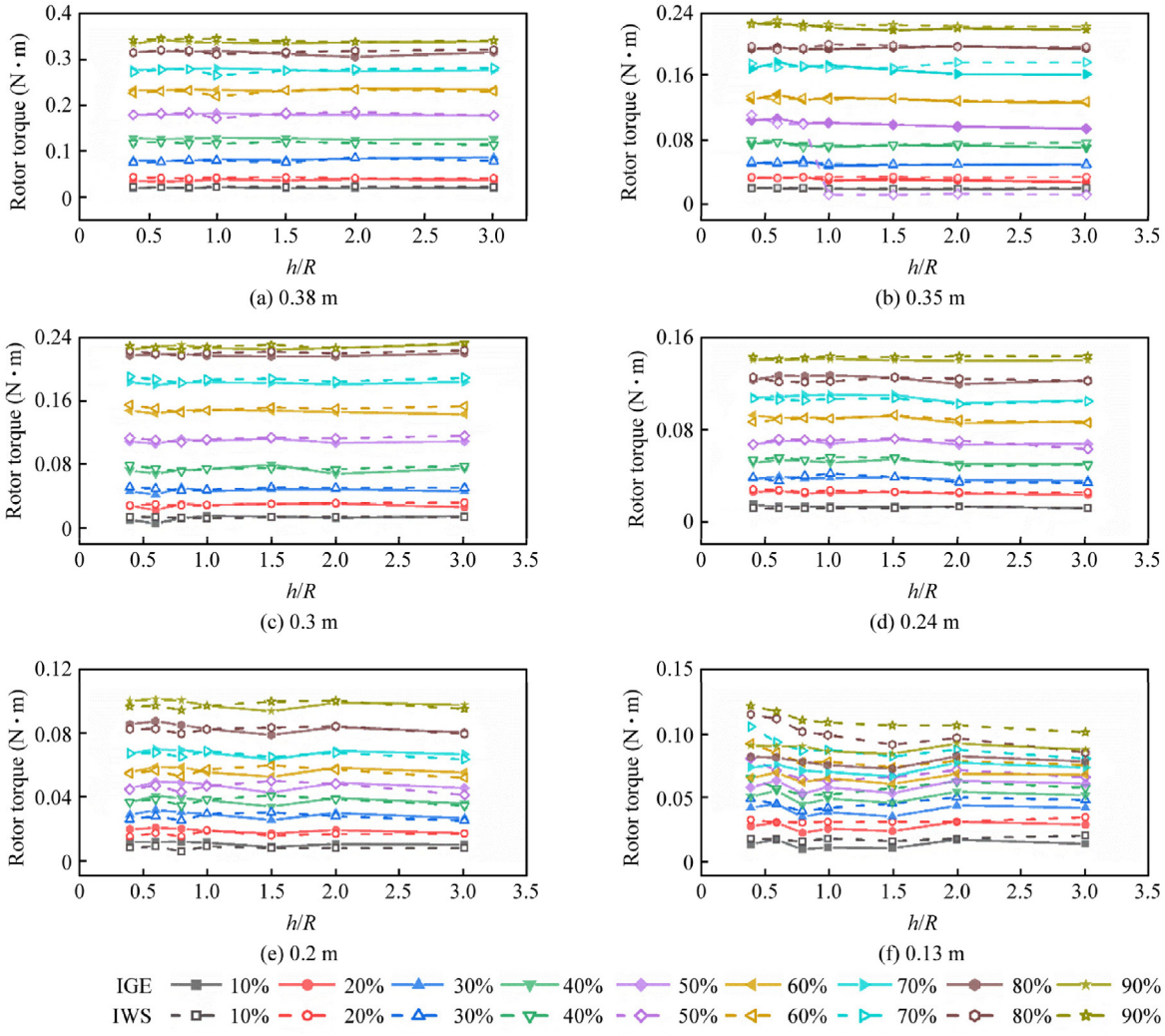

Fig. 8 Variation of rotor torque with parameter h/R.

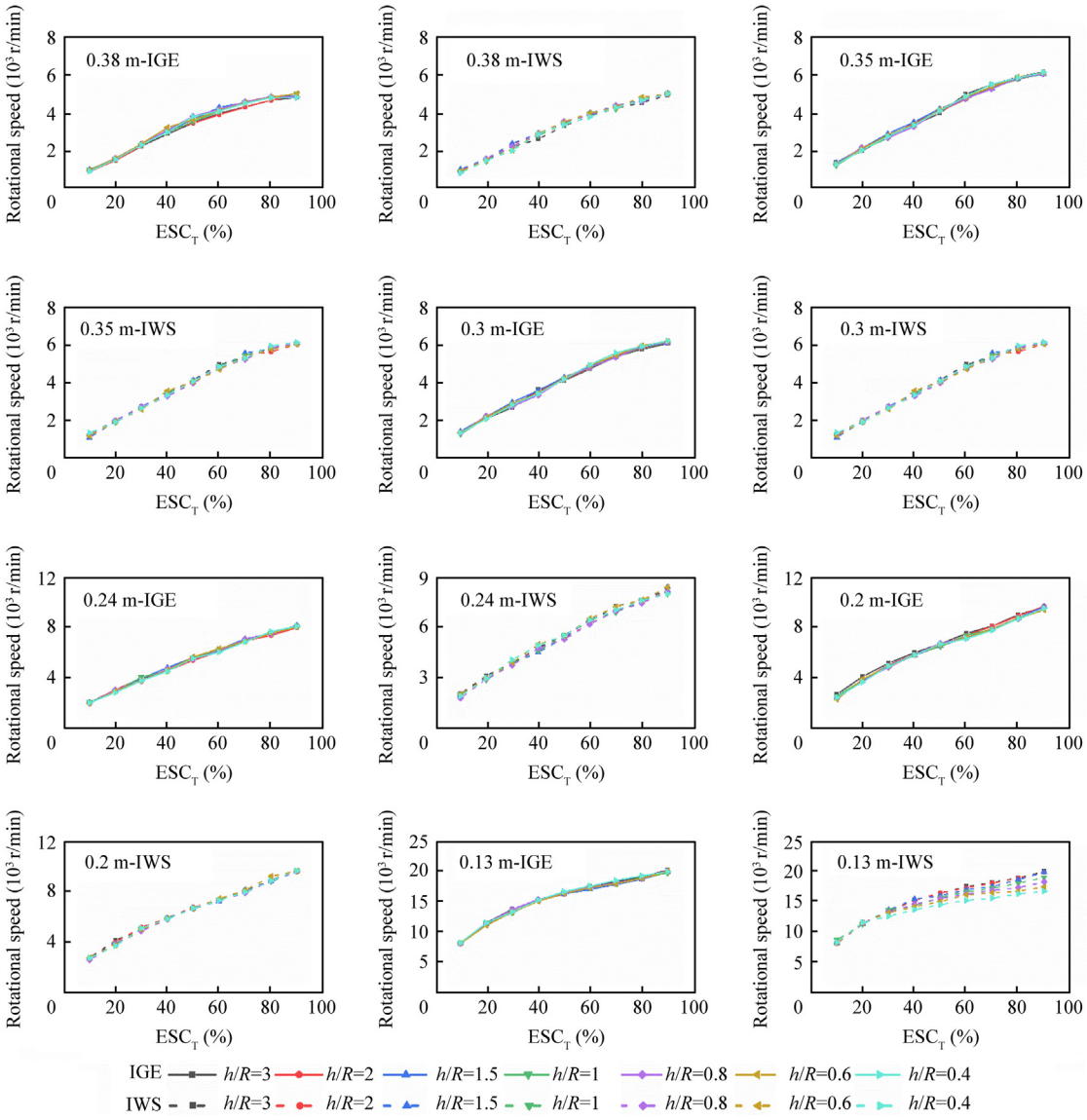

Fig. 9 Rotational speed of rotor with different sizes.

The third point occurs when $ESC_T > 40\%$ and $h/R < 1.5$; The fourth point occurs when $ESC_T > 50\%$ and $h/R < 2$; The fifth point occurs when $ESC_T > 80\%$.

(4) In addition, it can be noticed that the positive effect of the ground is greater than that of the water surface under the same conditions, as can be seen in Figs. 11(a)–(f).

Since phenomena 1 and 2 exhibit similar effects on the rotor aerodynamic performance, they can be consolidated into a single stage. Consequently, the evolution of the gas–liquid flow field when the rotor operating over water is attributed into two stages, as illustrated in Fig. 12. In the fountain stage, at a low ESC_T value, the water surface forms a depression under the impact of the rotor downwash, with fragmented droplets spreading outwards from the depression's edge. In the boiling stage, at a high ESC_T value, the water surface breaks up under the rotor downwash impact, with a large number of fragmented droplets being ejected into the flow field due to the rotor downwash.

3.2. Parameters optimization and model validation

In this subsection, an optimization of the FVRM is presented, and the predictive performance of the FVRM is validated with several aerodynamic methods.

The vortex ring filament with dimensionless circulation strength $\Gamma_u = 0.1$ is positioned at r (where r denotes the radius of the single vortex filament). Fig. 13(a) presents the induced velocity profile along the radial direction, revealing that the induced velocity increases as it approaches the r. Furthermore, the induced velocity exhibits a distortion near the r, with the induced velocity pointing downward outside the r and upward inside. By comparing different vortex core values, it can also be observed that as the value of δ approaches 0, the induced

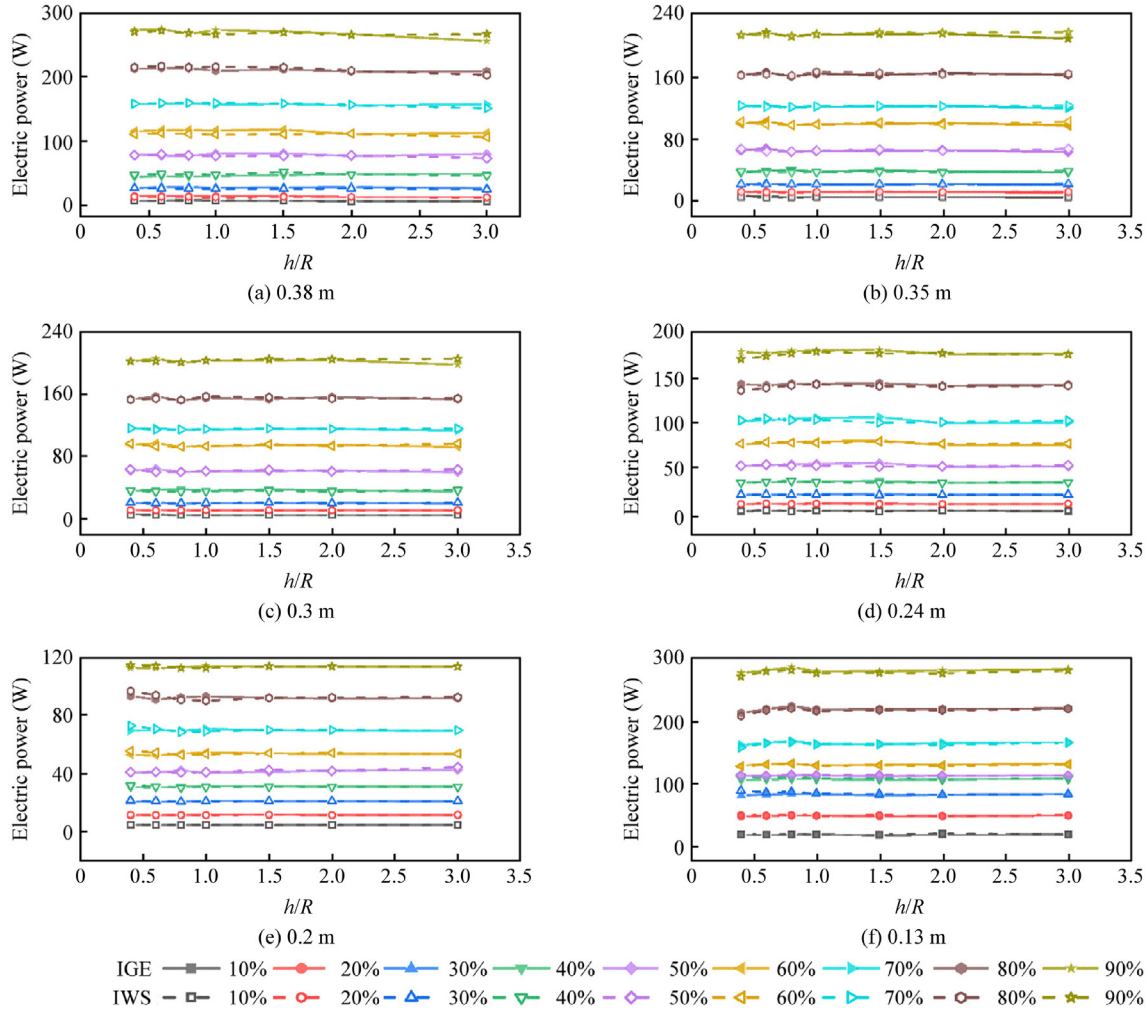

Fig. 10 Electric power of motor at different h/R.

velocity near the vortex ring filament approaches infinity. This is because when the δ approaches 0, the solution of Eq. (17) produces a singular solution. However, when the value of δ approaches the rotor radius R, the distortion of the rotor induced velocity at r reduced, and the profile of the induced velocity is closest to a uniform distribution. Fig. 13(b) demonstrates negligible sensitivity to circulation models, justifying the adoption of uniform circulation approximation for computational efficiency enhancement.

Fig. 14 illustrates the induced velocity on the rotor plane when the vortex strength is 0.1 and a uniform circulation distribution is assumed. As is shown in Fig. 14(a), with the rotor approaching the ground, the induced velocity increases from the tip to the root of the rotor along the radial direction. As is shown in Fig. 14(b), the induced velocity in the water effect increases from the tip to the root of rotor but fluctuates near the rotor center due to the deformation of the water surface. In the water effect, the distance between the image model and the rotor plane gradually changes along the rotor radial direction, which results in a distortion in the induced velocity distribution.

Fig. 15 presents the relationship between the water surface deformation of the deepest point (Δh_{dp}) with the impinging velocity in a fixed rotor initial altitude h_{init}. As evident from the Fig. 15, at a given height, the water depression depth exhibits an increase with the airflow velocity. Furthermore, at a constant airflow velocity, the water depression depth increases as the rotor height from the water surface decreases.

Fig. 16 depicts the deformation of the water surface (Δh) caused by the rotor downwash. The induced velocity on the rotor plane exhibits a non-uniform distribution, as illustrated in Fig. 14(b), resulting in a non-smooth water surface depression region. The reason is that the influence of the rotor hub was taken into account in the modelling, which makes a weak induced effect at the rotor root. However, the induced effect of the filament trailed by the other rotor segments persists, resulting in a non-zero induced velocity at $x/R = 0$. Specifically, the closer the position is to the rotor hub, the weaker the induced effect.

To further determine the value of δ ($0 < \delta < 1$), a rotor with a diameter of 0.38 m is taken as an example, and the prediction results of the FVRM model are compared with the experimental values. Furthermore, in order to quantify the results, a method for normalizing the prediction errors is presented. The percentage of mean-square error (P_{MSE}) related to the calculation results is defined as follows:

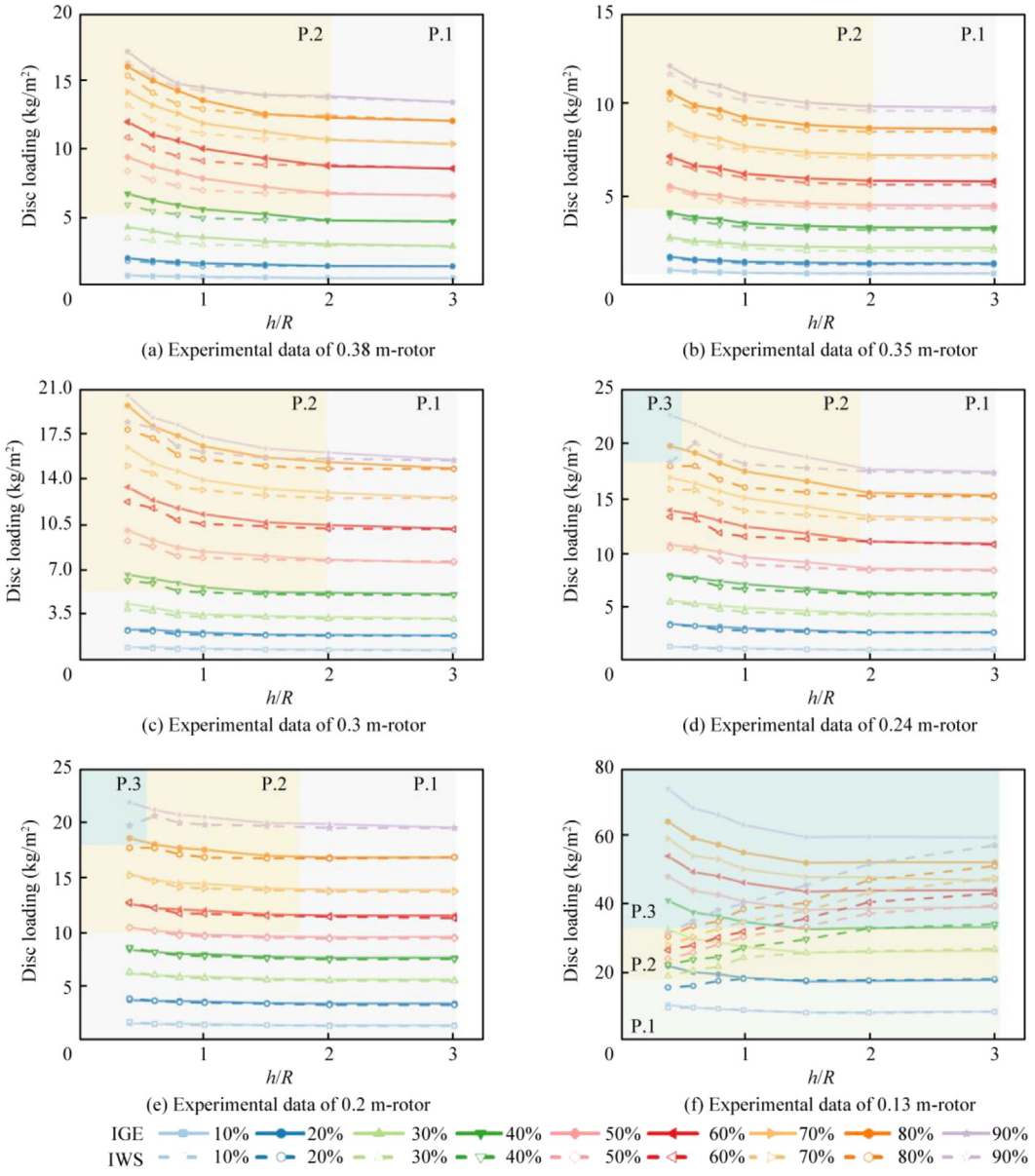

Fig. 11 Disc loading in the influence of ground and water.

Fig. 12 Evolution stage of gas–liquid flow field.

$$P_{\mathrm{MSE}} = \sqrt{\frac{1}{N}\sum_{i=1}^{N}\left[(E_{\mathrm{T}} - P_{\mathrm{T}})/E_{\mathrm{T}}\right]^2} \times 100\% \tag{43}$$

where P_{T} is the thrust of rotors in the prediction of FVRM.

It can be seen from Fig. 17 that as the value of δ approaches 0, the induced velocity near the vortex ring increases sharply, which in turn leads to an increase in the prediction error of

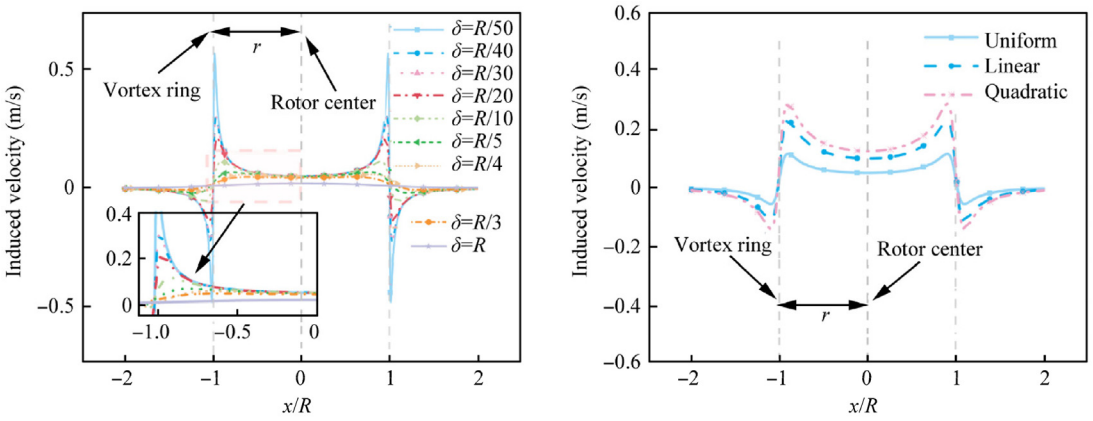

(a) Variation at different δ (b) Variation at different Γ_m model

Fig. 13 Comparison of induced velocity distribution.

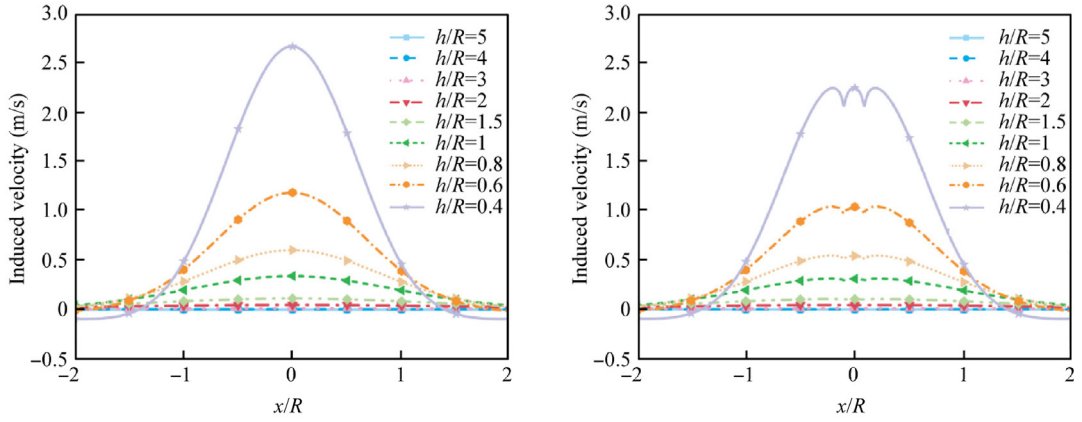

(a) In the influence of ground (b) In the influence of water surface

Fig. 14 Distribution of image induced velocity along rotor plane.

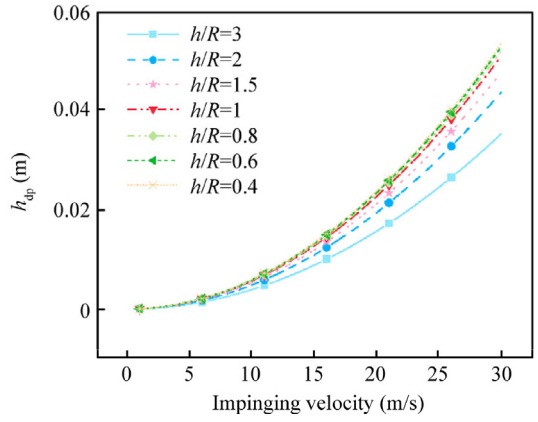

Fig. 15 Deformation of water surface with impinging velocity at different height.

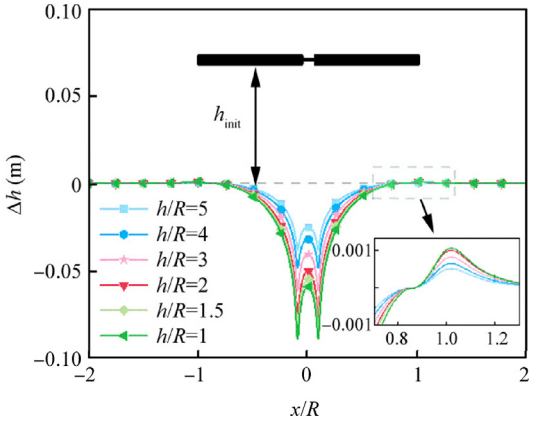

Fig. 16 Variation of water surface.

the FVRM model. When the value of δ approaches 1, the thickness of the vortex core is close to the rotor radius, making it impossible to accurately calculate the induced velocity generated by the vortex filament, resulting in the FVRM model being unable to obtain an accurate solution. Therefore, it can be concluded that the optimal value range of the vortex core thickness is 0.2–0.4. Among them, when the vortex core thickness is 0.2, that is $\delta = R/5$, the lower limit of the P_{MSE} approaches 0. At the same time, as can be observed from Fig. 13(a), when the value is $\delta = R/5$, the induced velocity is

closest to a uniform distribution, which means the induced power of the rotor is minimized.

Several prediction models are compared with the FVRM, such as the Cheeseman model, [27] the two-dimensional Potential Flow Model (PFM-2D),[19] and the three-dimensional Potential Flow Model (PFM-3D). [22] The rotor thrust prediction at the ESC_T values of 20%, 40%, 60%, and 80% under the influence of both water and ground is demonstrated in Fig. 18 and Fig. 19.

From Fig. 18 and Fig. 19, the results of the FVRM model demonstrate high accuracy in both the water effect and the ground effect. In contrast, for other models, the results deviate significantly from the experimental results when the rotor height above the ground is relatively small $h/R < 1$. The reason for this phenomenon is that in the Cheeseman, PFM-2D, and PFM-3D models, the calculation leads to a singularity when the height approaches 0. This problem is effectively addressed by the introduction of the vortex core δ in the FVRM model.

The prediction results of different models are summarized in Table 2, which reveals some findings as follow:

(1) The Cheeseman model, PFM-3D, and FVRM demonstrate satisfactory prediction accuracy in conventional ground effect conditions. However, in the extreme ground effect,[41] the prediction errors of both the Cheeseman model (P_{MSE} = 9.46%) and PFM-3D (P_{MSE} = 13.15%) exhibit progressive amplification. In contrast, the FVRM achieves enhanced predictive performance with an absolute error of 4.79% compared to experimental measurements. Finally, the average error of the FVRM achieves superior performance with a value of 6.94%. This enhancement is attributed to the adaptive strategy, which automatically modifies the model parameters in accordance with the rotor characteristics.
(2) In the influence of water, the FVRM model outperforms other models with significantly lower prediction error. At the ESC_T value of 20% (in the IWS), the FVRM model achieves prediction accuracy within 2.18%, maintaining the average error of 4.34%.

It is can be found that: (A) The Cheeseman model is simple and computationally efficient. However, its ability to accurately predict rotor thrust when subject to water surface disturbances is limited since it neglects rotor wake characteristics and circulation distribution. (B) The two-dimensional potential flow model incorporating the rotor wake is simple in structure and fast in computation, but the accuracy of the prediction needs improvement. (C) The three-dimensional potential flow model, a simplified vortex ring model, benefits from rapid computation but disregards the influence of the rotor circulation distribution, which fails in the thrust prediction concerning water interference. (D) The FVRM model considers rotor wake characteristics and water surface deformation to accurately predict rotor thrust near both the water and ground plane. Compared to other prediction models, FVRM offers high accuracy and low error rates while consuming fewer computational resources than traditional CFD method. However, its computational speed is slightly slower than the Cheeseman point source model.

3.3. Analysis of aerodynamic characteristics

Previous studies have demonstrated that the factors causing sudden lift drop are diverse, complex, and arise from multifactorial coupling. Thus, the DL, which is associated with the rotor's mass flow rate and downwash velocity, is introduced. In this section, the experimental results are compared with the FVRM model predictions, to investigate the relationship between DL and the water surface response, with the aim of identifying a transition boundary.

As illustrated in Fig. 20, the comparison between the experimental results and FVRM model predictions reveals a high degree alignment, which serve to indicate the FVRM model's high accuracy and reliability. Furthermore, the blue shaded area delineates the transition points at which rotor lift begins to decline. Once disc loading exceeds this threshold, the rotor thrust decreases. Thus, when the upward trend in lift shifts and the predicted lift intersects the experimental data, the flow field state transitions into the boiling stage.

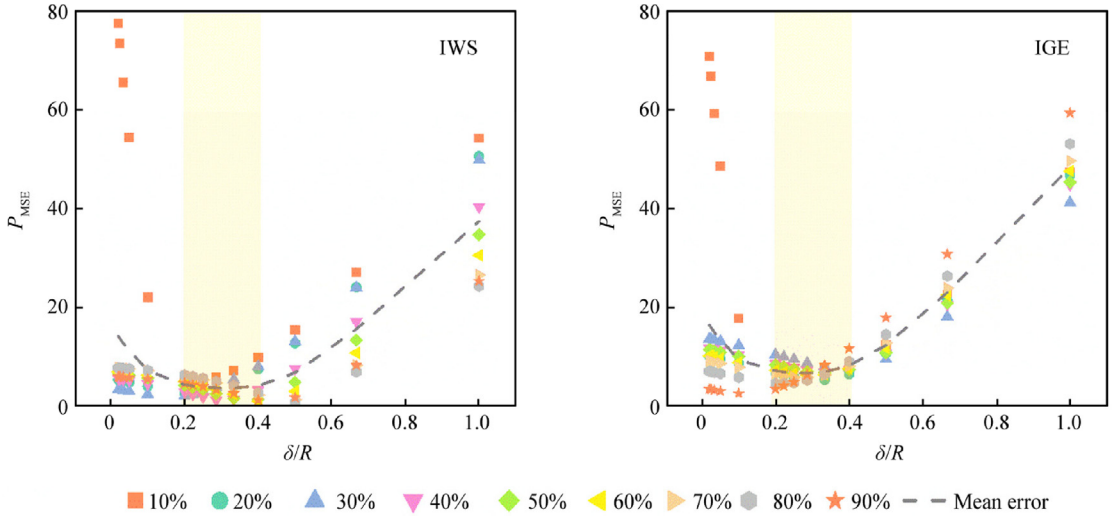

Fig. 17 P_{MSE} of FVRM prediction results.

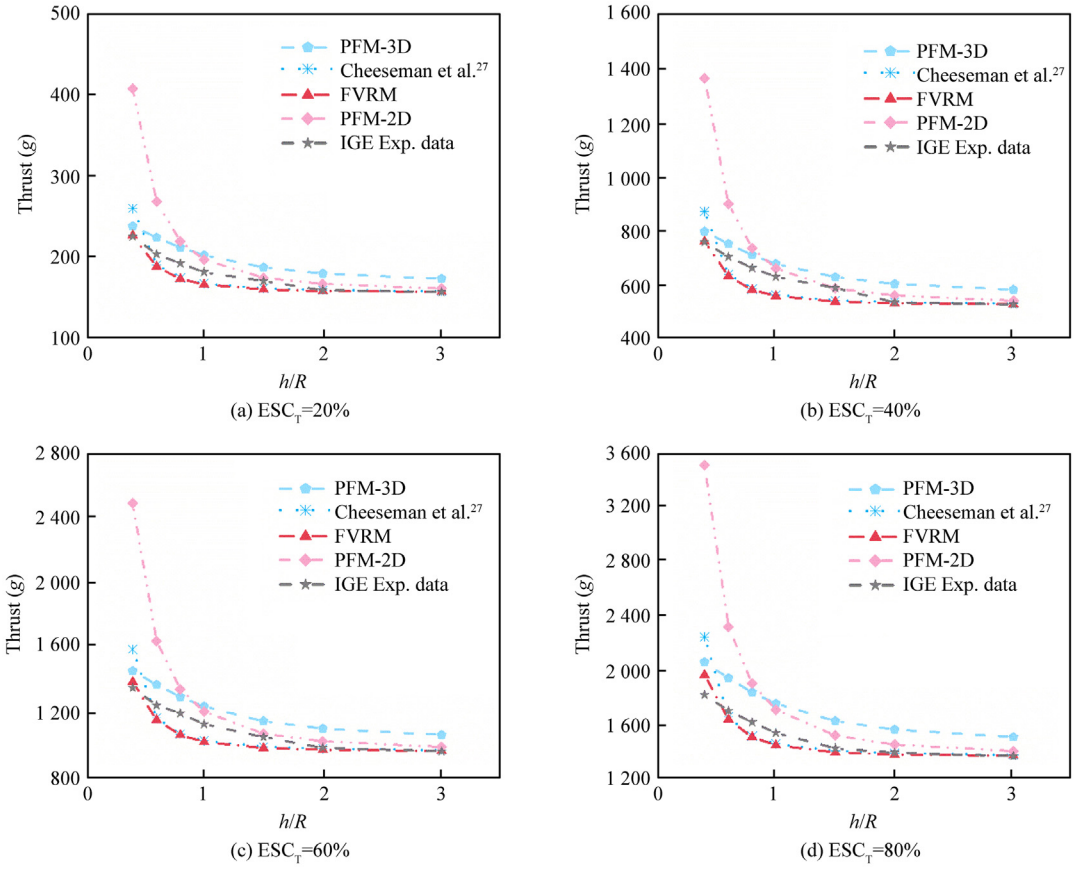

Fig. 18 Comparison of thrust predictions for 0.38 m-rotor under influence of ground.

According to current research, the reasons for the failure of the FVRM model during the boiling stage may be as follows: The downwash flow of the rotor impacts the liquid surface, generating a liquid crown and droplets. This causes an energy exchange between the rotor and the liquid surface, resulting in energy loss. Alternatively, the droplets form a uniform liquid film[48] that adheres to the rotor surface, which changes the aerodynamic shape of the rotor, making it difficult to predict the rotor's aerodynamic performance.

A method was proposed to fit the obtained data points based on the Farazdaghi-Harris model, the model is defined as

$$f(x) = (\alpha_f + \beta_f x^{\tau})^{-1} \tag{44}$$

where α_f, β_f and τ are constants obtained by the calculating and iterating based on the nonlinear regression of the Levenberg-Marquardt algorithm,[49,50] the $f(x)$ is the function of DL and the dimensionless height-to-radius ratio h/R.

Afterwards, some transition points were selected from Fig. 20, as shown in Table 3.

The experimental data were fitted based on the Farazdaghi-Harris model, and the corresponding fitting result is shown in Fig. 21.

In addition, the evolution boundary of the gas–liquid mixing state near the water surface of the rotor is given by numerical fitting. The transition boundary from fountain stage to boiling stage is defined as,

$$f(x) = (0.208 - 0.16(h/R)^{0.139})^{-1} \tag{45}$$

where $f(x)$ represents the transition boundary of the maximum range of the ESC_T and the disc loading in order to ensure the safe operation of the AAR near water. And, the safety range of AAR cruising near water is the region included in $f(x)$, as is marked in yellow in Fig. 22.

Fig. 22 presents a comparison of the experimental results with the transition boundary in different rotor sizes under near-water conditions, thereby demonstrating the reliability of the safety range. Within this range, the influence of water surface on the rotor performance resembles the ground effect; the closer the rotor is to the water, the stronger the lift enhancement. The rotor characteristics remain predictable in this range. Beyond this range, the rotor exhibits intense fluctuations, and the closer it is to the water, the stronger the negative impact on the rotor thrust, resulting in a reduction in lift. Moreover, increasing the rotor power further exacerbates the rotor lift loss. And, the rotor behavior under gas–liquid mixing conditions becomes irregular and unpredictable.

The transition boundary for gas–liquid flow field put forth was proposed as a potential means of facilitating the AAR design process. It is recommended that the design include an increase in the rotor disc area with the objective of reducing the disc loading, a limitation of the rotor power in proximity to the water surface, and an optimization of the controller strategy with the aim of preventing the occurrence of the boiling stage. Furthermore, the special boundary can also be extended into the AAR's rotor lift-altitude envelope.

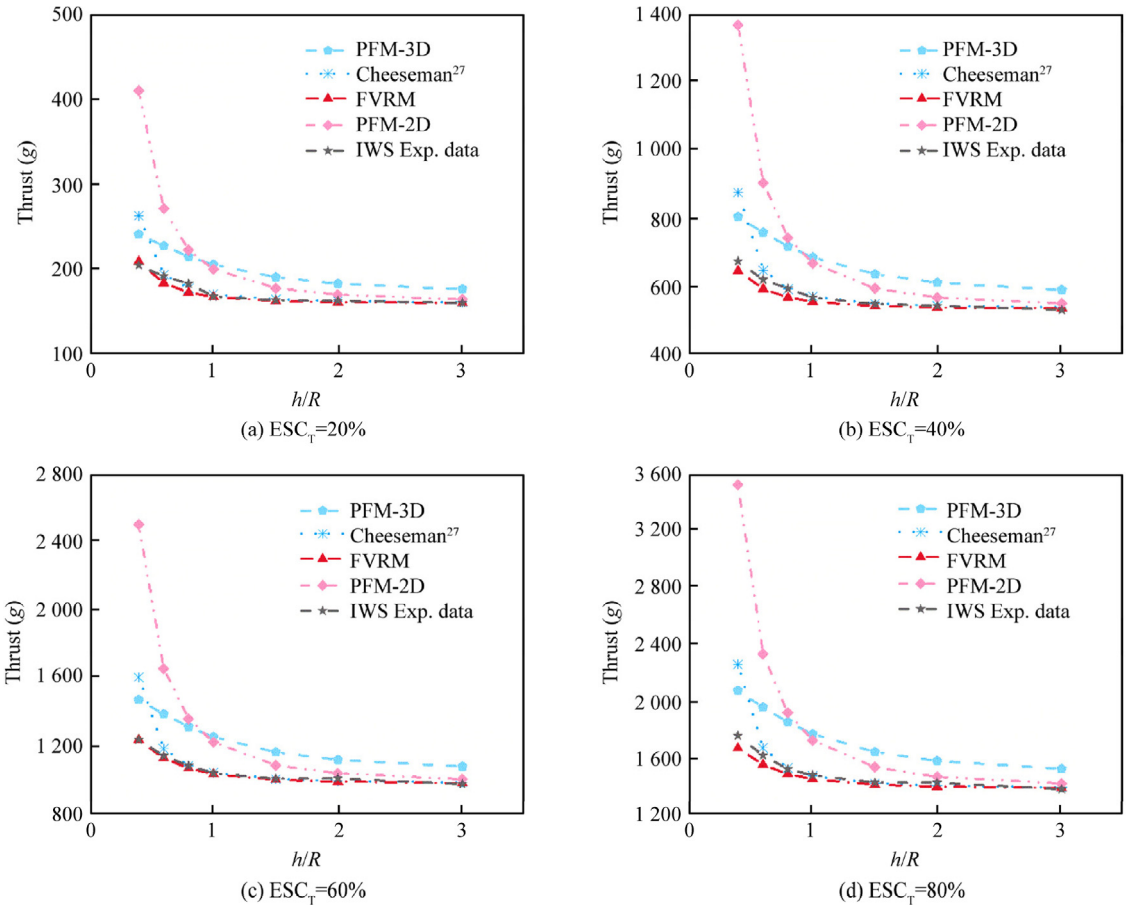

Fig. 19 Comparison of thrust predictions for 0.38 m-rotor under influence of water surface.

Table 2 Comparison of thrust prediction RMSE of different methods.

Hovering condition	ESC_T value(%)	Thrust P_{MSE} (%)			
		Cheeseman model	PFM-2D	PFM-3D	FVRM
Ground effect	20	7.87	32.98	10.11	6.88
	40	9.21	31.96	8.37	8.75
	60	8.92	34.09	9.68	7.34
	80	9.46	38.60	13.15	4.79
	Average P_{MSE} value	8.87	34.41	10.33	6.94
Interference of water surface	20	10.80	42.67	16.83	2.81
	40	11.53	44.47	18.07	3.00
	60	11.31	44.04	17.59	5.13
	80	10.99	43.56	17.37	6.4
	Average P_{MSE} value	11.16	43.69	17.47	4.34

It can be found that the primary factor influencing the rotor's near-water flow field is not rotor size, but the rotor's height above the water surface, along with the velocity and flow rate of the downwash. The analysis reveals that disc loading plays a critical role in determining the water surface state. When disc loading exceeds the threshold, it compels the flow field into boiling stage, even if the rotor is positioned at a considerable distance from the water surface. Therefore, in the design, the methods such as increasing the rotor disc area to reduce the disc loading, optimizing or limiting the rotor power near the water surface, and optimizing controller strategy are noticeably recommended to prevent the occurrence of boiling stage. Additionally, the transition boundary identified in this study can be incorporated into the AAR's rotor lift-altitude envelope to enhance operational safety and performance.

4. Conclusions

In this paper, a prediction model inspired by the finite element method was proposed to evaluate the aerodynamic perfor-

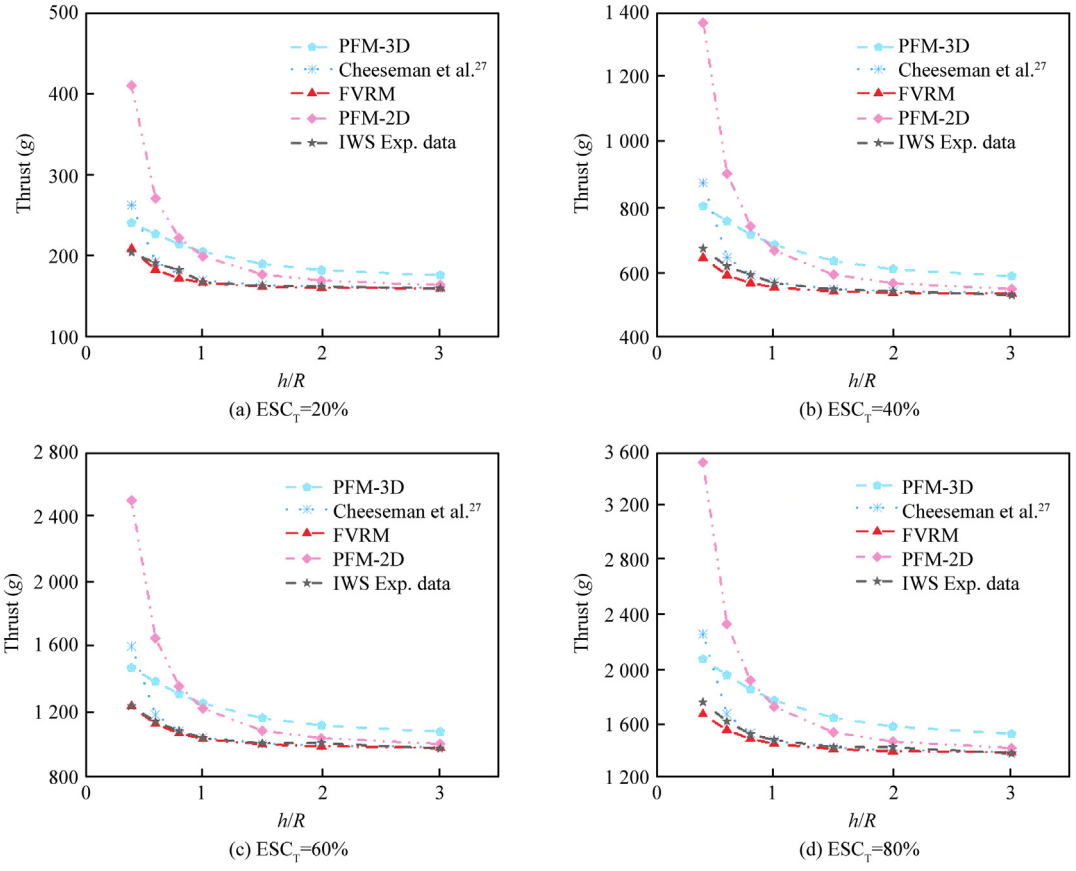

Fig. 20 Comparison of FVRM predictions and experimental data.

mance of aerial-aquatic rotorcraft, which takes into account the influence of the gas–liquid flow field. The following conclusions can be drawn from the investigation:

(1) The thickness of the boundary layer of vortex core has a significant impact on the induced velocity distribution. However, the various circulation models exhibit a negligible impact on the rotor induced velocity.

(2) The evolution of the water surface under the influence of the rotor wake can be categorized into three phenomena: Phenomenon 1 includes a depression on the water surface without droplet formation; Phenomenon 2 includes a deeper depression with a small number of droplets forming at the edge of the depression and splashing radially outwards along the rotor disc; Phenomenon 3 includes surging waves and obvious oscillations on the water surface, and the flow field is saturated with droplets and atomized droplets.

(3) The gas–liquid flow field can be classified into two stages, according to the influence of the water surface on the rotor performance. The fountain stage is characterized by a weak ground effect, with a predictable increase in the rotor thrust, including Phenomenons 1 and 2. In contrast, the boiling stage is a reverse ground effect, which results in an unpredictable decrease in the

Table 3 Data of transition points.

h/R	Disc loading (kg/m^2)
0.4	16
0.6	17
1	18
1.5	26
2	32
2.5	38
3	45

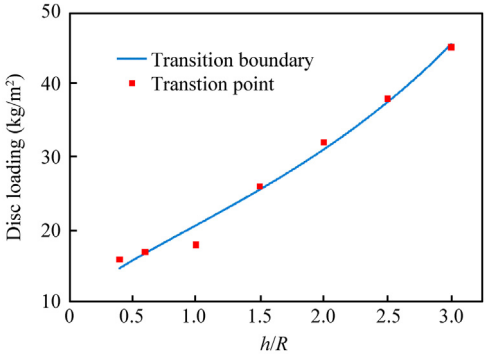

Fig. 21 Fitting results of transition points.

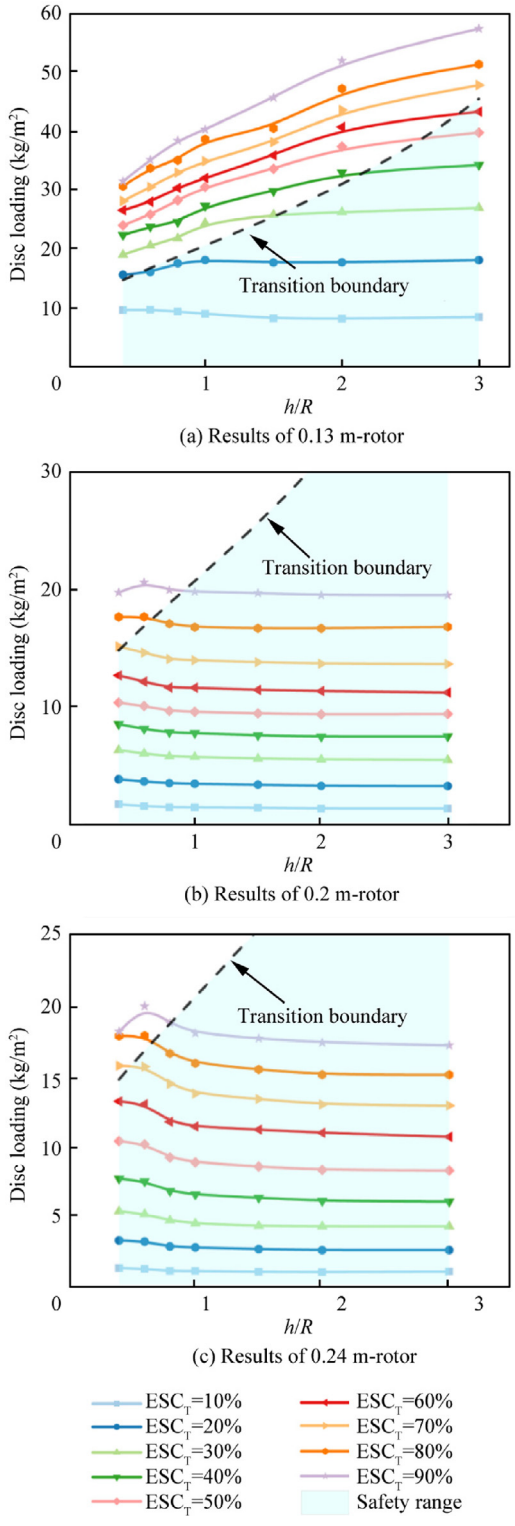

Fig. 22 Comparison of transition boundary and experimental data.

rotor thrust and a non-negligible influence on the aerodynamic performance during take-off and cruising operations above water.

(4) The models presented in this paper demonstrated an increase in the prediction error as the rotor height decreased, due to the gradual increase in the complexity of the rotor flow field. However, the FVRM model exhibited a superior predictive performance, regardless of whether the ground or water was considered. Moreover, the adaptive method used in the FVRM model resulted in an adaptive circulation strength, which is the critical factor in the prediction accuracy as the rotor approached water. Additionally, the FVRM model requires more computational power than the other methods.

(5) The transition boundary obtained based on the Farazdaghi-Harris model, has been proposed for potential utilization in the design of AAR and the control strategy. The accuracy and reliability of this boundary have been validated with various rotor sizes. The special boundary was proposed as a reliable range for the guidance in the design of the aerial-aquatic vehicles. In the preliminary design, a number of strategies were identified as being beneficial in preventing the occurrence of the boiling stage and ensuring safe flight near and crossing the water surface. These included increasing the rotor disc area to reduce the disc loading, optimizing or limiting the rotor power near the water surface, and enhancing controller robustness. Further research will be carried out in the future, based on the enhanced CFD and PIV techniques, with the aim of exploring the mechanism of the gas–liquid flow field of the AAR.

CRediT authorship contribution statement

Qi ZHAN: Writing – original draft, Validation, Software, Methodology, Investigation. **Xiao WANG:** Writing – review & editing, Conceptualization. **Junhui HU:** Writing – review & editing. **Xingzhi BAI:** Data curation. **Pierangelo MASARATI:** Writing – review & editing, Validation.

Declaration of competing interest

The authors declare that they have no known competing financial interests or personal relationships that could have appeared to influence the work reported in this paper.

Acknowledgements

The authors thank the Postgraduate Research & Practice Innovation Program of Jiangsu Province, China (No. KYCX24_0532), the Key Laboratory of Cross-Domain Flight Interdisciplinary Technology, China (Nos. 2024-KF03001, 2024-KF03003), and the National Natural Science Foundation of China (No. 12272169) for the financial support.

References

1. Yao GC, Li YZ, Zhang HY, et al. Review of hybrid aquatic-aerial vehicle (HAAV): Classifications, current status, applications, challenges and technology perspectives. *Prog Aerosp Sci* 2023;**139**:100902.

2. Zimmerman S, Abdelkefi A. Review of marine animals and bioinspired robotic vehicles: Classifications and characteristics. *Prog Aerosp Sci* 2017;**93**:95–119.
3. Li GR, Chen XP, Zhou FH, et al. Self-powered soft robot in the Mariana trench. *Nature* 2021;**591**(7848):66–71.
4. Zeng Z, Lyu CX, Bi YB, et al. Review of hybrid aerial underwater vehicle: Cross-domain mobility and transitions control. *Ocean Eng* 2022;**248**:110840.
5. Hassanalian M, Abdelkefi A. Classifications, applications, and design challenges of drones: A review. *Prog Aerosp Sci* 2017;**91**:99–131.
6. Li L, Wang SQ, Zhang YY, et al. Aerial-aquatic robots capable of crossing the air-water boundary and hitchhiking on surfaces. *Sci Robot* 2022;**7**(66):eabm6695.
7. Villegas A, Mishkevich V, Gulak Y, et al. Analysis of key elements to evaluate the performance of a multirotor unmanned aerial–aquatic vehicle. *Aerosp Sci Technol* 2017;**70**:412–8.
8. Lu D, Xiong CK, Zeng Z, et al. A multimodal aerial underwater vehicle with extended endurance and capabilities. *2019 international conference on robotics and automation (ICRA)*. Piscataway: IEEE; 2019.
9. Horn AC, Pinheiro PM, Grando RB, et al. A novel concept for hybrid unmanned aerial underwater vehicles focused on aquatic performance. *2020 Latin American robotics symposium (LARS), 2020 Brazilian symposium on robotics (SBR) and 2020 workshop on robotics in education (WRE)*. Piscataway: IEEE; 2020.
10. Horn AC, Pinheiro PM, Silva CB, et al. A study on configuration of propellers for multirotor-like hybrid aerial-aquatic vehicles. *2019 19th international conference on advanced robotics (ICAR)*. Piscataway: IEEE; 2019.
11. Weisler W, Stewart W, Anderson MB, et al. Testing and characterization of a fixed wing cross-domain unmanned vehicle operating in aerial and underwater environments. *IEEE J Ocean Eng* 2017;**43**(4):969–82.
12. Lu D, Guo YH, Xiong CK, et al. Takeoff and landing control of a hybrid aerial underwater vehicle on disturbed water's surface. *IEEE J Ocean Eng* 2022;**47**(2):295–311.
13. Aoki VM, Pinheiro PM, Drews-Jr PLJ, et al. Analysis of a hybrid unmanned aerial underwater vehicle considering the environment transition. *2021 Latin American robotics symposium (LARS), 2021 Brazilian symposium on robotics (SBR), and 2021 workshop on robotics in education (WRE)*. Piscataway: IEEE; 2021.
14. Zulu A, John S. A review of control algorithms for autonomous quadrotors. *OJAppS* 2014;**4**(14):547–56.
15. Matus-Vargas A, Rodriguez-Gomez G, Martinez-Carranza J. Ground effect on rotorcraft unmanned aerial vehicles: A review. *Intell Serv Robot* 2021;**14**(1):99–118.
16. Hsiao YH, Chirarattananon P. Ceiling effects for hybrid aerial–surface locomotion of small rotorcraft. *IEEE/ASME Trans Mechatron* 2019;**24**(5):2316–27.
17. Nakanishi H, Kanata S, Goto R, et al. Modeling and experimental validation for ceiling wall effect on aerodynamic characteristics of a rotor. *Artif Life Robot* 2022;**27**(4):734–42.
18. Hao JJ, Zhang YL, Zhou C, et al. Aerodynamic performance of hovering micro revolving wings in ground and ceiling effects at low Reynolds number. *Chin J Aeronaut* 2023;**36**(1):152–65.
19. Conyers SA. *Empirical evaluation of ground, ceiling, and wall effect for small-scale rotorcraft [dissertation]*. Denver: University of Denver; 2019.
20. Lee TE, Leishman JG, Ramasamy M. Fluid dynamics of interacting blade tip vortices with a ground plane. *J Am Helicopter Soc* 2010;**55**(2):22005–2200516.
21. Milluzzo J, Sydney A, Rauleder J, et al. In-ground-effect aerodynamics of rotors with different blade tips. *Annu Forum Proc AHS Int* 2010;**1**:697–720.
22. Calomiris D. *Potential flow model for wall-induced effects on propellers [dissertation]*. Montréal: McGill University; 2020.
23. Semenov IY. Development of hybrid air-water rotor transition thrust prediction and control [dissertation]. Maryland: University of Maryland; 2020.
24. Mi BG. Numerical investigation on aerodynamic performance of a ducted fan under interferences from the ground, static water and dynamic waves. *Aerosp Sci Technol* 2020;**100**:105821.
25. Wang JJ, Chen RL, Yu ZM, et al. Ground test and numerical investigation on aerodynamic performance of a quad tilt-rotor aircraft in ground and water effects. *Ocean Eng* 2023;**289**:116169.
26. Salazar R, Fuentes V, Abdelkefi A. Classification of biological and bioinspired aquatic systems: A review. *Ocean Eng* 2018;**148**:75–114.
27. Cheeseman IC, Bennett WE. The effect of the ground on a helicopter rotor in forward flight. London: Her Majesty's Stationery Office; 1957. Report No.: R. & M. No. 3021.
28. Pulla DP. *A study of helicopter aerodynamics in ground effect [dissertation]*. Columbus: The Ohio State University; 2006.
29. Liang H, Zong Z, Zou L. Nonlinear lifting theory for unsteady WIG in proximity to incident water waves. Part 1: Two-dimension. *Appl Ocean Res* 2013;**43**:99–111.
30. Liu XA, Ma DL, Yang MQ, et al. Numerical study on airfoil aerodynamics in proximity to wavy water surface for various amplitudes. *Appl Sci* 2021;**11**(9):4215.
31. Sugiura M, Tanabe Y, Sugawara H, et al. Numerical simulations and measurements of the helicopter wake in ground effect. *J Aircr* 2016;**54**(1):209–19.
32. Ji DX, Wang XW, Wang R, et al. Simulation of vertical water exit of rotor unmanned aerial, underwater vehicle based on STAR-CCM+. *2021 WRC symposium on advanced robotics and automation (WRC SARA)*. Piscataway: IEEE; 2021.
33. Tan JF, Zhou TY, Wang C, et al. Aerodynamic model and characteristics of rotor in ground effect. *Acta Aeronautica et Astronautic Sinica* 2019;**40**(6): 122602 [Chinese].
34. Wang TQ, Liu L, Li J, et al. Time-history performance optimization of flapping wing motion using a deep learning based prediction model. *Chin J Aeronaut* 2024;**37**(5):317–31.
35. Sanchez-Cuevas P, Heredia G, Ollero A. Characterization of the aerodynamic ground effect and its influence in multirotor control. *Int J Aerosp Eng* 2017;**2017**:1823056.
36. Joseph S, Benjamin B, William G, et al. Experimental study of rotor performance in deep ground effect with application to a human-powered helicopter. *Proceedings of annual forum of the American helicopter society*, 2012.
37. Milluzzo JI, Leishman JG. Vortical sheet behavior in the wake of a rotor in ground effect. *AIAA J* 2016;**55**(1):24.
38. Lee H, Sengupta B, Araghizadeh MS, et al. Review of vortex methods for rotor aerodynamics and wake dynamics. *Adv Aerodyn* 2022;**4**(1):20.
39. Zhao YF, Geng LB, Yang Y, et al. Research on aerodynamic characteristics of a ducted propeller hovering near the water surface based on a lattice Boltzmann method. *J Mar Sci Eng* 2023;**11**(9):1708.
40. Cottet GH, Petros K. *Vortex methods - theory and practice*. Cambridge: Cambridge University Press; 2000. p. 1–62.
41. Wu ZL, Zhang TY, Tan HJ, et al. Hovering rotor aerodynamics in extreme ground effect. *Chin J Aeronaut* 2024;**37**(7):204–19.
42. Kim C, Park D, Noh KC, et al. Velocity and energy conversion efficiency characteristics of ionic wind generator in a multistage configuration. *J Electrost* 2010;**68**(1):36–41.
43. Hwang HY, Irons GA. A water model study of impinging gas jets on liquid surfaces. *Metall Mater Trans B* 2012;**43**(2):302–15.
44. Qian F, Mutharasan R, Farouk B. Studies of interface deformations in single- and multi-layered liquid baths due to an impinging gas jet. *Metall Mater Trans B* 1996;**27**(6):911–20.
45. He AD, Belmonte A. Deformation of a liquid surface due to an impinging gas jet: a conformal mapping approach. *Phys Fluids* 2010;**22**(4):042103.

46. Banks RB, Chandrasekhara DV. Experimental investigation of the penetration of a high-velocity gas jet through a liquid surface. *J Fluid Mech* 1963;**15**(1):13–34.
47. Cheslak FR, Nicholls JA, Sichel M. Cavities formed on liquid surfaces by impinging gaseous jets. *J Fluid Mech* 1969;**36**:55–63.
48. Li GZ, Cao YH. Numerical simulation of helicopter rotor performance degradation in natural rain encounter. *Int J Aerosp Eng* 2021;**2021**(1):5533823.
49. Umar AO, Sulaiman IM, Mamat M, et al. On damping parameters of Levenberg-Marquardt algorithm for nonlinear least square problems. *J Phys: Conf Ser* 2021;**1734**(1):012018.
50. Gavin HP. The Levenberg-Marquardt algorithm for nonlinear least squares curve-fitting problems [dissertation]. Durham: Duke University; 2024.